The Brain/MINDS 3D Digital Marmoset Brain Atlas Version 2.0: Population-based Cortical Region Parcellations with Multi-Modal Standard Templates

Rui Gong[1,2], Noritaka Ichinohe[3], Hiroshi Abe[4], Toshiki Tani[4], Mengkuan Lin[5], Takuto Okuno[6], Ken Nakae[7], Junichi Hata[6,8,9], Shin Ishii[2], Patrice Delmas[10], Shahrokh Heidari[10], Jiaxuan Wang[10], Tetsuo Yamamori[4], Hideyuki Okano[8,9], and Alexander Woodward[1]

[1]Connectome Analysis Unit, RIKEN Center for Brain Science, Wako, Saitama, Japan
[2]Integrated Systems Biology Laboratory, Department of Systems Science, Graduate School of Informatics, Kyoto University, Kyoto, Japan
[3]Department of Ultrastructural Research, National Center of Neurology and Psychiatry, Kodaira, Tokyo, Japan
[4]Laboratory for Molecular Analysis of Higher Brain Function, RIKEN Center for Brain Science, Wako, Saitama, Japan
[5]Department of Neurobiology, University of Pittsburgh School of Medicine, Pittsburgh, PA, United States
[6]Graduate School of Human Health Sciences, Tokyo Metropolitan University, Tokyo, Japan
[7]Graduate School of Engineering, University of Fukui, Fukui, Japan
[8]Laboratory for Marmoset Models of Brain Diseases, RIKEN Center for Brain Science, Wako, Saitama, Japan.
[9]Keio University Regenerative Medicine Research Center, Kawasaki, Kanagawa, Japan
[10]Intelligent Vision Systems Laboratory, The University of Auckland, Auckland, New Zealand

ABSTRACT

We present the Brain/MINDS population-based 3D digital brain atlas version 2.0 (BMA2.0), a population-based 3D digital brain atlas of the common marmoset (Callithrix jacchus), designed to overcome limitations of previous single-subject atlases that are prone to structural biases arising from individual variation. This release integrates manually delineated cortical regions from 10 myelin-stained brains to generate a generalized cortical parcellation. Subcortical regions from a previous version (BMA2017) and a state-of-the-art cerebellum atlas (University of Pittsburgh) were also incorporated, resulting in a comprehensive whole-brain parcellation of 636 regions. To enhance cross-modal registration accuracy, we implemented artificial intelligence (AI)-based techniques, including CycleGAN and Pix2Pix for image translation and segmentation. These methods enabled accurate alignment across myelin, Nissl, block-face, and MRI modalities by providing both visual similarity and anatomically meaningful constraints. The atlas package includes population-average templates for myelin and Nissl staining (based on 10 individuals), a new ex vivo MRI standard space constructed from 91 brains, and an in vivo average brain from 446 individuals. Additionally, flat map projections and surface models (outer, mid, and inner cortical layers) are provided, facilitating multi-modal integration and spatial analysis. While applications such as quantification of laminar thickness are demonstrated, BMA2.0 is designed as a general-purpose platform for cross-modal registration, data integration, and comparative neuroscience. It supports spatially grounded analysis of marmoset brain structure and function and offers broad compatibility with existing datasets and software.

Background & Summary

The Brain Mapping by Integrated Neurotechnologies for Disease Studies (Brain/MINDS) project[1] was launched in 2014 by the Japan Agency for Medical Research and Development (AMED) in collaboration with an extensive network of research institutions. The Brain/MINDS project was a decade-long endeavor that sought to deepen our understanding of the networks of the brain. Using the common marmoset (Callithrix jacchus) as a model animal, the project was intended to both improve our understanding of neuroscience and help develop new diagnostic tools and treatments for brain-related illnesses.

In this work, we introduce the Brain/MINDS digital 3D marmoset brain atlas version 2.0 (BMA2.0), a fully symmetrical, population-based cortical atlas constructed from ten individual marmoset brains. This atlas aims to provide a more realistic representation of brain regions within the common marmoset population compared to existing atlases based on a single brain. In addition, several average brain templates have been developed, including ex vivo, in vivo T2-weighted (T2WI) MRI, myelin, and Nissl. These templates can simplify the process of image registration to the atlas, enabling research and data analysis using

the available data from these modalities, as image registration between different modalities can be challenging.

The common marmoset is a small New World monkey that has come to be regarded as a valuable model animal due to its close phylogenetic relationship to humans[2,3], its relatively small size, and its short gestation period. The present study has found that the subject is used extensively in scientific research, particularly in studies related to neuroscience, including but not limited to genetics[4], and brain-related diseases such as Alzheimer's[5–7], neuro degeneration[8,9], and reproductive biology[10,11]. As neuroscience research continues to explore the complexities of brain structure and function, the development of a comprehensive brain atlas for the common marmoset becomes very important.

A brain atlas is a reference framework that provides a systematic representation of the brain's anatomical structures. The brain atlas enables researchers to locate and identify brain regions, study neural circuitry, connectivity, and function of these regions[12,13]. Due to the amount of work needed to delineate and construct even a single brain atlas, a population-based atlas is considered the 'Holy Grail' of brain atlases. Creating a population-based marmoset brain atlas is a challenging task, as it involves integrating information from various imaging modalities and different histological techniques. To make some of these tasks more manageable, we have incorporated various AI-based computational methods into our construction pipeline.

We have previously released two marmoset brain atlases, the Brain/MINDS digital marmoset brain atlas 2017 (BMA2017)[14] and the Brain/MINDS digital marmoset brain atlas 2019 (BMA2019)[15]. These atlases are available to the public through the Brain/MINDS data portal[1]. The first release, the BMA2017 atlas, was based on a single brain[16,17], where the brain regions were annotated in the left hemisphere only, using Nissl contrast with 114 cortical regions per hemisphere. The second release, the BMA2019 atlas, introduced a population-average T2WI ex vivo MRI brain template based on the same region annotation as the BMA2017 atlas. Both atlases have been used in several important marmoset brain studies, including the prefrontal cortex circuits study by Watakabe et al.[18], and the Brain/MINDS NA216 (in vivo) and eNA91 (ex vivo) MRI database by Hata et al.[19]. While those two releases have improved our understanding of the structures of the marmoset brain, the inherent brain structural bias among individuals may not provide the most accurate representation of different brain regions, as brains within a population can vary in size, shape, and anatomical structure.

Other existing marmoset brain atlases, such as the population-based cortical template by Majka et al.[20], provide a similar population-based cortical atlas, but, it is limited by only using the region delineations on the left hemisphere based on Nissl histology data, which is then mapped onto a population average Nissl template without other more commonly used modalities such as T2WI MRI, making it difficult to register. The marmoset brain mapping atlas version 3 (MBMv3) by Liu et al.[21] offers a valuable template by integrating two existing atlases, the marmoset brain mapping atlas version 1[22] and our BMA2017[14]. However, its application is constrained by the utilization of only two atlases, a limitation that hinders the sufficient diversification necessary to mitigate potential biases associated with individual variability.

For our BMA2.0 release, we have constructed a population-based cortical atlas of the marmoset brain, integrating data from 10 individual atlases, which collectively delineate 117 cortical regions per hemisphere. We employed a streamline-based methodology to assign the most probable label to each streamline within the cerebral cortex, while accounting for both the left and right hemispheres. This is combined with the subcortical regions from BMA2017 (156 regions) and a new cerebellum region atlas (45 regions), resulting in a total of 323 regions per hemisphere, providing the most comprehensive brain region coverage to date. This population-based atlas aims to capture the diversity of a population's brains and give a more average shape of each cortical brain region by incorporating 10 individual brain atlases. This enables a more comprehensive understanding of the common marmoset's brain, its organization, and its functions.

While previous atlases have focused on a single imaging modality or contrast, BMA2.0 uniquely integrates both Nissl and myelin staining within a common 3D coordinate space. These two histological modalities offer complementary laminar signatures: Nissl reveals cytoarchitectonic features based on neuronal cell body distribution. At the same time, myelin highlights fiber architecture through laminar patterns such as the middle band. This dual-modality integration allows cross-validation of laminar features and supports population-level morphometric analyses. Furthermore, it establishes a robust anatomical framework for multi-modal registration, facilitating comparison with in vivo MRI, tracer-based connectivity data, and spatially resolved molecular techniques such as spatial transcriptomics.

Our population-based marmoset brain atlas is then mapped onto a new symmetrical T2WI ex vivo MRI population average template based on 91 individuals from the eNA91 dataset. We have also created Myelin and Nissl contrast average templates based on histological data from those 10 individuals, as well as a new in vivo T2WI population average template derived from 446 individuals in the NA216 dataset, which is also mapped onto our new MRI average template space. This provides researchers with different modalities for registering, analyzing, and comparing their data using our new atlas. We also provided image transforms from BMA2.0 space to our previous releases, BMA2017 and BMA2019, so that analysis conducted within these releases can be easily transferred.

Beyond serving as a reference framework, the multi-modal nature of our dataset also enables morphometric studies. In particular, we leveraged the laminar contrast observed in myelin-stained sections to quantify the variation in thickness

[1] https://dataportal.brainminds.jp

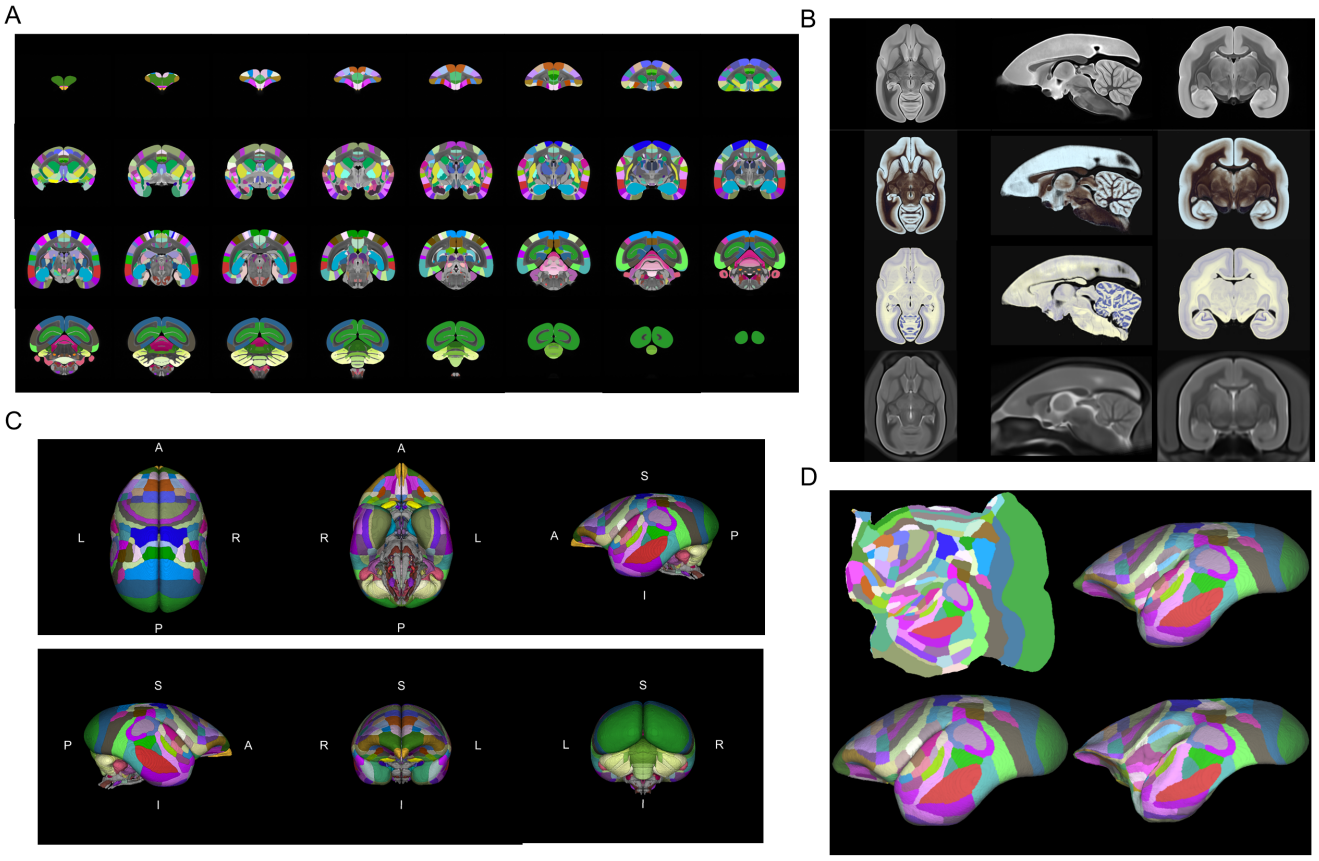

Figure 1. Overview the BMA2.0 package. (A) Coronal views of the BMA2.0 population-based atlas (117 cortical regions, 156 subcortical regions and 45 cerebellum regions per hemisphere) from anterior to posterior with 20 slices intervals, mapped onto the BMA2.0 T2WI population average template. (B) Axial, sagittal, and coronal views of BMA2.0 population average T2WI MRI (N=91), myelin (N=10), Nissl (N=10), and in vivo T2WI (N=455) template. (C) 3D reconstruction of BMA2.0 atlas, from top left to bottom right: superior, inferior, left hemisphere, right hemisphere, anterior and posterior views, respectively. (D) From top left to bottom right: left hemisphere cortical flat map, left mid-cortical surface, left pial surface, and left white matter surface with BMA2.0 atlas label mapping.

of layers 1-3 across the cerebral cortex. While high-magnification Nissl staining is often used to define cortical layers, it may be insufficient at lower resolutions due to the variable cell density in layer 4 and the intense staining in large layer 5 neurons. In contrast, the myelin-stained middle band provides a more consistent and reliable laminar signature at the resolution used for population-based mapping. Using this signal, we observed systematic dorsal-ventral and rostral-caudal gradients in supragranular thickness, highlighting the biological richness of our atlas and its potential for comparative cortical studies.

The development of a population-based marmoset brain atlas represents a significant advancement in our understanding of marmoset brain structure and function. The main goal of our BMA2.0 release as a comprehensive package, is to serve as a state-of-the-art reference resource for researchers, enhancing our understanding of the complexities of the common marmoset brain. This atlas is expected to advance the field of neuroscience while simultaneously offering insights with potential implications for human brain health and disease research.

Methods

Data acquisition and histological annotation

In this section, we provide an overview of all the data used for BMA2.0 atlas and template construction, as well as how they were obtained.

Brain slicing and staining protocols

The data acquisition process for each marmoset brain is as follows. The brain was initially placed on dry ice, after which coronal brain sections were sliced along the axial plane at a thickness of 50 µm. Every third section was then collected for

different histological processing, The sections were assigned in a repeating sequence in the following order, myelin staining, Nissl staining, and tracer imaging, where the tracer images are taken in three distinct channels (F/T/C). This alternating scheme (myelin-Nissl-tracer) ensured that the histological series were evenly spaced at regular intervals throughout the brain, enabling multimodal analysis across comparable anatomical levels. A more detailed explanation is provided in Abe et al.[23]. Data on the 10 marmosets used in this work are as listed in Table 1.

Marmoset ID	Age (yr) at Perfusion	Body Weight (g) at Perfusion	Birth Date	Sex
I1514	2.4	344	2013.09.23	F
I1515	4.8	-	2011.05.06	F
I1607	2.1	389	2014.04.26	F
I1611	2.6	298	2014.04.06	M
I1614	6.3	352	2010.10.22	F
I1701	5.5	299	2011.10.17	F
I1703	3.3	346	2014.03.11	F
I1704	3.1	280	2014.08.22	M
I1709	2.0	339	2013.12.12	F
I1804	6.4	-	2012.02.19	F

Table 1. Data of the 10 Marmosets used for constructing the population-based atlas.

Block-face imaging and ex vivo MRI acquisition

Block face data for each brain was taken after each slice along the axial plane using a camera mounted at a fixed position on top. The total number of block face images produced by each brain was approximately 600. More details are provided in Table 2.

Ex vivo T2WI MRI scan of the 10 adult marmosets was acquired using a 9.4-T BioSpec 94/30 unit (Bruker Optik GmbH, Ettlingen, Germany) and a transmit and receive coil with an inner diameter of 86 mm. A more detailed explanation of the data acquisition process can be found in Hata et al.[19].

Marmoset ID	Number of Block face Images	Number of Myelin Images	Number of Nissl Images
I1514	632	211	211
I1515	573	191	191
I1607	600	200	200
I1611	600	199	200
I1614	627	209	209
I1701	555	185	183
I1703	600	199	200
I1704	566	187	187
I1709	614	205	204
I1804	561	187	187

Table 2. Data of images need to be processed and registered for population-based atlas construction, population average myelin-stained and population average Nissl-stained templates.

Manual delineation of cortical regions on myelin-stained slices

The delineations of the cortical region were identified by neuroanatomists and drawn onto every individual myelin-stained tissue slice (150 microns between each myelin-stained slice) in both hemispheres, for 10 individuals. Two histological techniques were used to help identify brain regions, myelin-staining (fiber tracts) and Nissl staining (cell bodies), in conjunction with the reference border definitions and nomenclature provided by Paxinos marmoset brain atlas[12].

Manual background segmentation

The background segmentation, which is used to separate brain tissue from background, was manually drawn for all myelin (1/3 of block face slices) and block face slices (roughly 600 slices) of the 10 brains. This segmentation information was later used in our processing pipeline in two ways: first, as additional constraints for image registration, and second, as training data for artificial intelligence (AI) algorithms for image segmentation tasks.

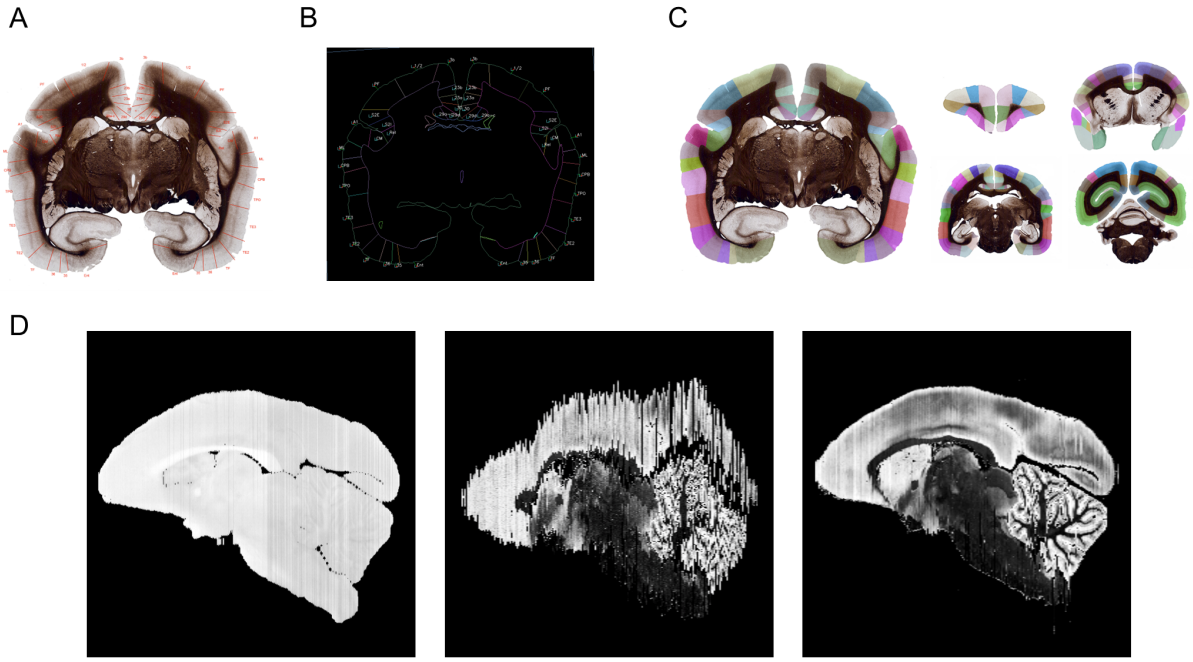

Figure 2. Example of NanoZoomer pipeline image conversion and image registration. (A) Region delineations identified by neuroanatomists with region borders drawn onto myelin histology. (B) Output of converted machine-readable region delineations using our Nanozoomer image process pipeline. (C) Converted region delineations overlay onto the original myelin images. (D) Examples of image registration of myelin to block face in sagittal view, comparing myelin volume before and after image registration. From left to right, block face volume, myelin volume before image registration, and myelin volume after image registration.

Convert cortical region delineations to machine-readable format

Myelin images, along with their corresponding cortical region delineations, were first processed using our NanoZoomer image processing pipeline (NZP)[15], which converts region delineation drawings (in SVG format) into 2D TIFF images with their respective region labels. Example outputs from our pipeline are shown in Figure 2B and Figure 2C. 16-bit grayscale values were assigned to each region, representing its region number using a region lookup table as defined in the BMA2017 and BMA2019 releases.

Following the machine conversion of the region delineations for all the slices, manual reviews were conducted to identify and rectify any errors that occurred during the conversion process. We identified conversion errors, including incorrect region assignments, multiple region assignments to the same regions, and unenclosed region borders. Such problems were fixed manually and then reprocessed using our pipeline. In instances where region delineations were absent due to damaged or missing tissue, the missing slice was replaced by a duplicate of the previous slice. This manual checking process ensured the correct region delineation conversions for all slices (approximately 200 per brain) across all 10 brains.

Image registration pipeline

In this section, we describe the process of 2D and 3D image registration using Advanced Normalization Tools, and AI-based image processing techniques to enhance the accuracy of image registration.

2D and 3D registration using ANTs

Image registration is a challenging problem in the fields of computer vision and medical imaging. The objective involves aligning images, whether of the same or different modalities, into a reference coordinate system. This is achieved through the implementation of affine and nonlinear image warping techniques, which establish a spatial correspondence between the pixels or features present in the images. This is one of the most important processes of digital brain atlasing, as we need to restore histological data, including myelin and Nissl, to their original block face shape using 2D image registration. 3D image registration is also used to transform between individual block face volume and ex vivo MRI volume, as well as to map all 10 individual brain atlases into a common standard brain template. As shown in Figure 2D, stacking myelin-stained images without image registration results in an unaligned brain volume compared to its original block face volume, and this is restored after image registration.

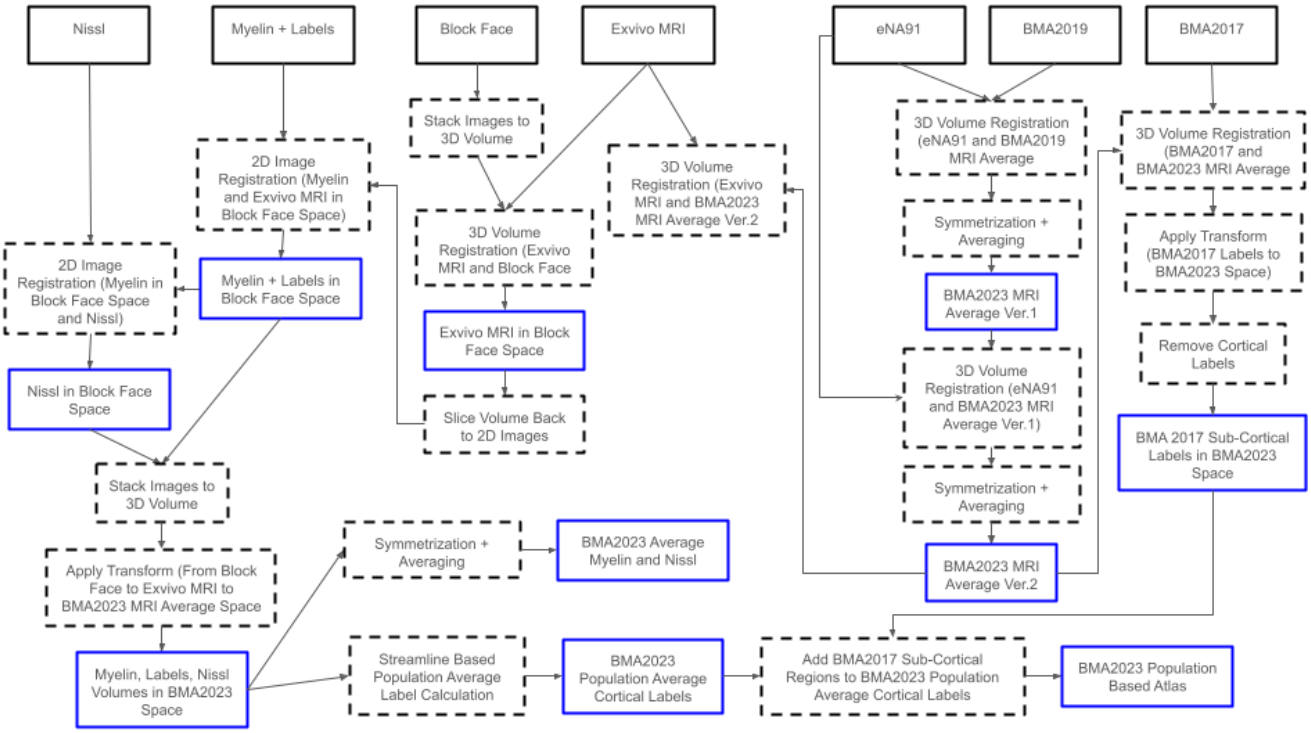

Figure 3. Overview of BMA2.0 population-based atlas and average templates construction. Black squares indicate all the available original data source, dotted squares indicate image processing applied, and blue boxes indicate outputs.

One of the popular tools used for image registration is the Advanced Normalization Tools (ANTs)[24,25], which contains tools for various image processing tasks, and most importantly, supports deformable, multi-modal, and high-dimensional image registration tasks. For our work, we used ANTs version 2.4.4 ("Eotapinoma", released May 2nd, 2022) to perform both 2D image and 3D volume image registrations, using mainly 2 registration shell scripts (antsRegistrationQuick.sh and antsRegistrationSyN.sh), which were executed under the Ubuntu version 22.04 operating system.

AI-based image processing techniques for improving image registration

In recent years, machine learning and artificial intelligence have emerged as popular and powerful techniques for addressing traditionally ill-posed problems in the field of computer vision. In this section, we describe the various Artificial Intelligence (AI) algorithms used to accomplish computer vision tasks such as image space translation between myelin and Nissl, cortical and subcortical region segmentation of myelin images, and brain tissue and background segmentation. These techniques were used to enhance the accuracy of image registration across different image modalities (myelin, Nissl, T2WI MRI, and block face) by either providing additional information, such as cortical boundary constraints, or translating images into similar modalities. In image registration, additional segmentation constraints function as landmarks on the images, providing the registration algorithm with information on the areas and regions that should be matched.

Image space translation of Nissl to myelin

Due to the distinctiveness of color and contrast between myelin and Nissl images, it is very challenging to perform image registration to accurately match the internal brain structure between them. To improve the accuracy, we decided to use an AI algorithm to translate Nissl images into myelin-like color and contrast.

The algorithm we decided to use is a Generative Adversarial Network (GAN) based algorithm, which is a machine learning framework that can automatically detect and learn the regularities or patterns in input data. It is capable of generating new samples that are indistinguishable from the original dataset. CycleGAN, a popular unpaired image-to-image translation model developed by Zhu et al.[26]. The primary benefit of this algorithm is that it eliminates the need for image pairing during the training process, thereby simplifying the preparation of training images for the algorithm.

To prepare the training data for CycleGAN, we used myelin and Nissl images from 10 marmoset brain datasets (around 200 myelin and Nissl images per individual). Initially, all original myelin images were resized to align with the dimensions of the background segmentation images, as the original myelin images were acquired at extremely high resolution using NanoZoomer

(55000×55000 pixels), and the manual segmentation was drawn under significantly lower resolution.

Background segmentation is then applied to myelin images to remove background noise, such as liquids and parts of brain tissue from other slices. Manual background segmentation was not performed on the Nissl images, so the training dataset for Nissl included background artifacts, such as fragments of brain tissue from adjacent slices, liquid residual, etc. in some images.

Next, we applied padding to each image in the training set to ensure that all images were the same square size. For each brain, we first find the max length or height (σ_{max}) from all the myelin images, to keep the relative physical size for all the images. Zero padding is applied to pad each image into a square size, with new length and height = σ_{max}, while keeping the brain tissue at the center. Finally, all padded image is then resized to 512×512. The same padding process is used for Nissl images as well.

We have used image augmentations to increase the number of training images in our limited datasets. Image augmentation is a technique for the artificial generation of image data for machine learning tasks, as machine learning networks typically rely on large datasets to prevent overfitting[27]. Overfitting occurs when the network perfectly models the training data, which can yield accurate results using the training data, but struggles to produce good results with unseen data. For the image augmentation task, we have used the Python package Argumentor[28].

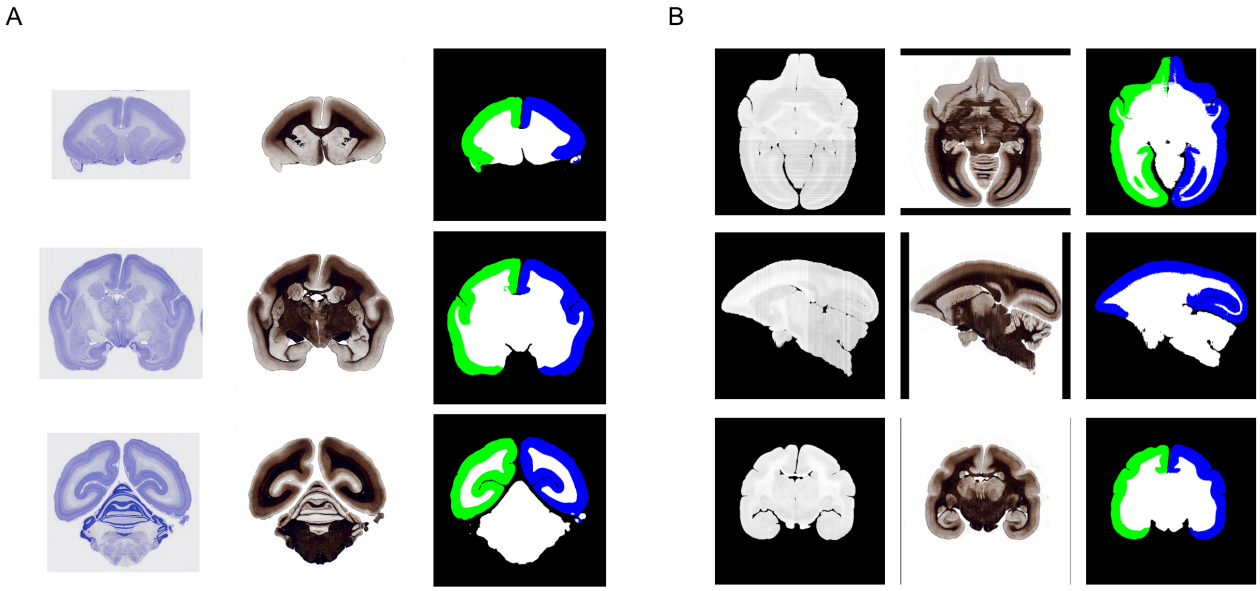

Figure 4. Example outputs of image translation using CycleGAN and cortical segmentation using Pix2Pix (A) From left to right: examples of synthetic myelin images generated from Nissl using CycleGAN. Then, from synthetic myelin images, cortical segmentation is generated using Pix2Pix'. (B) From left to right: an example of a whole synthetic myelin volume generated from images from a block face volume using CycleGAN, followed by a cortical segmentation volume generated from the synthetic myelin volume using Pix2Pix. Blue, green, white and black represent the left cerebral cortex, the right cerebral cortex, non-cortical areas and the background respectively in the axial, sagittal and coronal views (from top to bottom) for figures A and B.

The augmentations applied to the myelin and Nissl image training include zooming and image rotations, which help increase the total number and variety of training images, making the training of CycleGAN more robust. In total, we used 9261 myelin and Nissl images to train the network. Some examples of Nissl images that are translated to synthetic myelin images generated from our trained CycleGAN network are shown in Figure 4 A.

Cortical boundary segmentation of translated Nissl

To further improve the accuracy of image registration, we can include additional constraints, such as segmentation, in conjunction with images for image registration[29]. This works by providing additional information to help identify general regions to be matched during image registration. In the case of Nissl to myelin image registration, we would like to include segmentation masks that identify several brain regions: cortical regions (left and right), subcortical regions, and background, to guide the matching of relevant brain regions during the registration process.

To create the cortical boundary segmentation images, we employed Pix2Pix, a GAN-based algorithm first introduced by Isola et al.[30], to train and generate the left/right cortical boundary and subcortical segmentation for myelin contrast images.

Compared to CycleGAN, Pix2Pix learns a mapping from an input image to an output image based on paired examples, meaning Pix2Pix requires the preparation of training images by pairing each myelin image with its corresponding segmented mask.

To prepare training segmented mask data, we first generated cortical and subcortical boundary segmentation from cortical region delineation data generated from our NanoZoomer pipeline, and then combined it with background segmentation data. To generate left/right hemisphere cortical boundary segmentation from cortical region delineations, we first identified the center of the image and then assigned either the left or right hemisphere to each region based on which side it is on. We manually corrected any incorrect assignments in the output for all slices. Next, we combined the left/right cortical segmentation with background segmentation information to identify subcortical regions and backgrounds. We assigned 4 color codes, blue, green, white, and black, representing left hemisphere cortical regions, right hemisphere cortical regions, subcortical areas, and background, respectively.

We then paired the original myelin images with the cortical segmentation images (images from 6 brains, 1181 image pairs in total), then used Argumentor[28] to apply rotation and zoom to both myelin and segmentation image pairs to get a total number of 8192 image pairs and used them to train the Pix2Pix network.

Lastly, we used the trained network to generate cortical boundary segmentation using synthetic myelin images derived from Nissl, as shown in Figure 4 A, providing additional segmentation constraints to improve image registration from Nissl to myelin.

Image space translation of block face to myelin

To enhance the accuracy of image registration from myelin to block face images, we also used CycleGAN, similar to the Nissl to myelin image translation. To prepare training images, we first applied background segmentation to remove background noise and brain tissues from other slices from myelin images, and day ice from block face images. Padding is then applied to all images based on each brain.

Our primary goal is to translate block face images into myelin-like textures, thereby mitigating registration challenges caused by the lack of texture in block face images. However, due to inconsistencies within the cerebellum region and layer 4 in the cortical regions of the synthetic myelin images generated from block face images. We did not use those images for registration, as such results can warp the cerebellum and the cerebral cortex from real data in unexpected ways. This problem is mainly caused by the lack of texture in the block face images within the cerebellum area, where our network had to perform 'guess' work rather than relying on textures. This problem did not occur in Nissl to myelin translation due to the well-defined texture within the Nissl cerebellum.

Still, synthetic myelin from block face was used to generate cortical boundaries as described in the next section, which is then used to guide the 3D volume registration of the individual MRI to the block face.

Cortical boundary segmentation of translated block face

We used the trained Pix2Pix network to generate cortical segmentation for each slice of synthetic myelin, which was converted from block-face data using CycleGAN. The first step is to convert the cortical segmentation results to a volumetric format for each of the 10 brains in block face space. An example of synthetic myelin volume from block face to cortical segmentation using Pix2Pix is shown in Figure 4 B. The volumetric segmentation separates cortical regions, subcortical regions, and background for each brain, which is then used to guide the 3D registration of individual MRI volumes to individual block face volumes by utilizing the segmentation as markers. The 3D volume registration ensures the alignment of structure delineations between individual block face volumes and individual MRI volumes for each brain.

Background removal of Nissl

To further improve the image registration accuracy of Nissl to myelin images, we aim to separate brain tissue from the background, as the background contains noise such as liquid or brain tissue from another slice, which affects registration accuracy around the edges of the brain. However, unlike myelin, manual background segmentation was not made for Nissl images.

To generate the background segmentation for Nissl, we took advantage of the myelin image training set for CycleGAN, which already incorporates background segmentation into the images. This means that our trained CycleGAN network, using this training set, can generate synthetic myelin images with clear backgrounds from Nissl. An example of this can be seen in the synthetic myelin images generated from Nissl images, which are shown in Figure 4.

Therefore, all we need to do is take the synthetic myelin images translated from Nissl and extract the background segmentation using a straightforward threshold technique, where pixels that are white or close to white are considered background. A small challenge of this approach is that while it effectively addressed the removal of the background, it did not automatically eliminate extra tissues sometimes present in the Nissl images. For such images, we manually inspect and remove any extra brain tissue. This is then used to remove background noise in Nissl, allowing image registration to focus exclusively on the relevant anatomical details without interference from the background.

Atlas and templates construction

In this section, we describe the process of constructing the population-based atlas using streamline-based method and multi-modal population-based average templates.

Population average standard MRI brain template construction

In our BMA2.0 dataset, we have created a new population average T2WI ex vivo MRI brain using data available from the Brain/MINDS data portal, specifically the eNA91 dataset by Hata et al.[19]. The eNA91 data set contains ex vivo MRI scans of a subset of 91 individuals with an average age of 5.27 ± 2.39 years. We used the T2WI MRI brains from the eNA91 for the population average brain construction.

To create the new ex vivo MRI population average, all 91 individual brains were first registered to our previous population average MRI brain from BMA2019 using ANTs, which has a volume size of $300 \times 360 \times 220$ voxels at a resolution of 100 µm. This gave us 91 individual brains in the BMA2019 space. For the new MRI population average template of BMA2.0, we would like to make it truly symmetrical to eliminate the possible bias between the left and right hemispheres. To achieve this, we first made each registered brain in the eNA91 dataset symmetrical. A more detailed description can be found on our Brain/MINDS data portal's tutorial section [2]. We first flip each brain volume along the sagittal plane, and then register each flipped brain volume to the original brain volume. Next, we calculate halfway transforms for both forward and backward transforms. The halfway transforms are then applied to the flipped and original brain volumes, which transform both brains into an almost symmetrical 'halfway' shape. Lastly, we take the average of the two brains to create individual symmetrical brains, which accounts for the information from both the left and right hemispheres on each side.

The first version of the BMA2.0 population average template was made by averaging those 91 symmetrical brains. To achieve true symmetry, we flipped the left hemisphere along the sagittal axis to obtain a symmetrical population average template in the new BMA2.0 space (version 1).

To further refine the BMA2.0 population average template, we registered 91 individual brains to the BMA2.0 population average template version 1 and then repeated the averaging process. This gave us a slightly more refined version of the BMA2.0 population average template. Areas such as the lateral sulcus were improved compared to version 1. This refined version is used as the new standard space for our BMA2.0 (version 2). The resolution of our new BMA2.0 average MRI is the same as BMA2019, $300 \times 360 \times 220$ pixels, with a voxel size of 100μm resolution.

Individual and Average MRI cortical boundary segmentation and registration

To accurately transform data from the 10 individual spaces (region labels, myelin, and Nissl) to the new BMA2.0 space, it is ideal to perform registration between data with similar modalities. Since our BMA2.0 average template is constructed from ex vivo T2WI data, we decided to first register the T2WI MRI volumes of the 10 individuals to the average template. To further improve the accuracy of 3D volume registration, we need additional registration constraints such as cortical boundary segmentations.

Firstly, to obtain this segmentation information for both individuals and the BMA2.0 population average template, we used existing cortical segmentation information from BMA2019, where manual segmentation was performed to segment several brain regions, including the left and right hemispheres of the cerebral cortex, white matter, internal structures, and cerebellum. Next, we registered the 10 individual MRI volumes to the BMA2019 average MRI brain using ANTs. Then, we applied the resulting transformations to map the region segmentation of BMA2019 back to the 10 individuals, which provided an initial mapping of brain region segmentation for all 10 individual MRI brains. To improve the accuracy of segmentation mapping, we manually checked and edited the transformed region segmentation for each of the 10 individual brains using the segmentation editor module from 3D Slicer[31] (version 5.2.2 was used in our work) [3] to fix errors in segmentation mappings from image registration.

We used the same process to create cortical boundary segmentation for BMA2.0, first registering the BMA2019 average template to the new BMA2.0 average template and then applying transforms to transform the segmentation from BMA2019 to BMA2.0 space. The segmentation was then also manually edited using 3D Slicer to fix errors in the mapping.

Lastly, we used ANTs to register each of the 10 individual MRI volumes to the BMA2.0 average template with segmentation constraints, thereby achieving a more precise alignment of segmented regions through image registration. The resulting transforms allow us to transform data between individual MRI space and BMA2.0 average template space.

Iterative image registration of individual myelin to individual block face

Now that we have the transforms between individual MRI space and the BMA2.0 average template space, we next need to obtain the transformation from individual myelin/region labels to the original brain shape. This can be achieved by using either block face or T2WI MRI data, as both datasets maintain the original brain shape. Ideally, we want to register myelin to T2WI

[2] https://dataportal.brainminds.jp/tutorial-how-to-make-a-symmetric-brain
[3] https://www.slicer.org/

MRI, as myelin and T2WI MRI exhibit very similar contrast in grayscale images. However, this is challenging because we lack positional information to match each myelin slice with the corresponding MRI slice, which is only maintained in block-face data. Therefore, we first need to establish a correspondence between the individual MRI and the individual block face, which can be achieved by using image registration.

To obtain an accurate registration between individual MRI volumes and individual block face volumes, we first stacked individual block face images and their corresponding cortical boundary segmentations into 3D volumes and then registered them to individual MRI volumes with cortical boundary constraints. We then use the transforms to transform individual MRI volumes to block face space, allowing us to convert them back to 2D images. This gave us MRI contrast images for each block face slice, with slice numbering matching the corresponding myelin and Nissl image data.

We first performed image registration of individual myelin images to MRI images in block face space, using the slice number to match corresponding image pairs. Myelin and MRI images exhibit similar textures to the internal structures of the brain slice when compared to textureless block face images. After the initial registration, we stacked registered myelin images and their cortical segmentation into a 3D volume using 3D Slicer, which gave us a myelin volume (registered myelin volume iteration 1) and a cortical segmentation volume of myelin in its individual block face space.

However, due to the lower resolution of the MRI images e.g. $300 \times 360 \times 100$ pixels with a voxel size of $100\mu m \times 100\mu m \times 200\mu m$, compared to block face's e.g. $500 \times 500 \times 600$ pixels with a voxel size of $67.2\mu m \times 67.2\mu m \times 50\mu m$, interpolation was used after transforms, resulting in regions such as the cerebellum not registering well from this step.

To improve the registration in those areas, we applied a 3D median image filter with radius size 1 to the transformed myelin volume. This step blurs the volume, reducing noise between slices in 3D (specifically in the cerebellum region) while preserving structural boundaries, this give us a blurry myelin contrast brain that we can use for image registration again. We sliced the blurred myelin volume again into coronal plane images and performed registration from the original myelin images to the blurred myelin with a cortical segmentation constraint. As the images now have similar contrast, this step provided a much better registration of the internal structures in the myelin images. Again, we stack the registered myelin images into a 3D volume (registered myelin volume iteration 2).

We then take the registered 3D myelin volume (iteration 2) from the previous step and register it in block face space to the MRI volume, adjusting the alignment of internal structures. This ensures that myelin slices align correctly in 3D space. Then, we apply this transform, zero out one dimension (AP-axis), and apply it to the 3D myelin volume, so that the slices are not shifted along the AP-axis while maintaining the alignment of internal structures.

Next, we applied a 3D median image filter again with a radius of 1 to blur the myelin volume. We then sliced the blurred volume into coronal plane images and repeated the image registration from the original myelin to the blurred myelin images. Finally, we stacked the registered myelin images back to a 3D volume, which gave us the registered myelin volume in individual block face space (registered myelin volume iteration 3).

Myelin average template construction

For this release, we aim to provide modalities other to T2WI to ease data registration to our BMA2.0 average space. One of them is a population-based myelin average brain based on 10 individuals.

We applied ANTs transforms to first align myelin slices to block face space, stack the transformed images into a 3D volume, and then apply compound transforms (individual block face to individual MRI, individual MRI to BMA2.0) to align the myelin volume to the BMA2.0 template space. To increase the total number of brains and to make the template more symmetrical, we flipped each of the 10 myelin brains to get a total number of 20 myelin brains. We then constructed the myelin average contrast brain by applying averaging over those 20 myelin brains. The resolution of the BMA2.0 average myelin-stained brain is $300 \times 360 \times 220$ pixels, with a voxel size of $100\mu m \times 100\mu m \times 100\mu m$.

Nissl average template construction

Another modality we would like to provide in this release is an average Nissl brain template. To make the average Nissl-stained brain, we first registered synthetic myelin from Nissl to the myelin images in block face (from the final stage of myelin to block face registration) space with cortical segmentation. We then apply the transforms to the original Nissl images and stack the transformed images into a 3D volume to create Nissl volumes in block face space. We then applied transforms from individual block face space to individual MRI, then to the BMA2.0 population average space.

We then flipped the 10 transformed Nissl brains to get a total of 20 brains and averaged them. This gave us an initial version (version 1) of the average Nissl-stained brain. However, we wanted to make some further improvements because the initial step was performed using synthetic myelin from Nissl for the image registration process, which yielded better registration results compared to registering Nissl to myelin. Still, it could potentially omit some unique features from the original Nissl-stained images.

To improve upon this, we repeated the image registration process by registering individual Nissl to the BMA2.0 average Nissl version 1. For this step, we first applied inverse transforms to transform the average Nissl-stained brain back to the

individual block face space. Then we sliced the 3D volume into 2D images, each representing the original block face image in the same position. We then registered each Nissl image to its corresponding average Nissl image in the individual block face space. Registered images were then stacked back into 3D volumes and transformed back to the BMA2.0 average space using the same transform path from individual block face space to the population average. Again, we flipped the 10 brains to obtain 20 brains in total and performed averaging to create the second iteration of the average Nissl-stained brain template. Compared to the Nissl average from iteration 1, the second iteration of the Nissl average appears less blurry. It has a more precise definition of layer 4 within the cerebral cortex, as well as a more distinct cerebellum. The resolution of the BMA2.0 average Nissl-stained brain is $300 \times 360 \times 220$ pixels, with a voxel size of $100\mu m \times 100\mu m \times 100\mu m$.

In vivo average template construction

Another important aspect of the marmoset brain templates is the inclusion of in vivo brain data, as resting-state fMRI and structural connectivity studies[32–34] rely on in vivo data, and manual skull-stripping is required as a pre-processing step in such studies. By providing an in vivo template, the process of skull stripping can be made easier or even unnecessary if the goal is to map the atlas to the data.

On the Brain/MINDS data portal, an in vivo marmoset population average standard template is provided with the NA216 data set[19]. In this work, we have made a new in vivo standard template based on our BMA2.0 space. The main challenge is registering in vivo data to our BMA2.0 average template, due to the inclusion of the skull in the in vivo data. To overcome this challenge, we took the existing in vivo NA216 average template (n=216), made it symmetrical, and manually segmented the brain tissue to strip the skull using 3D Slicer's segmentation tools. Then, we take this in vivo brain without the skull and register it to our BMA2.0 average template. The resulting transforms are then used to transform the in vivo average template with the skull into our BMA2.0 space.

We then took all the individual in vivo data (N=455), registered it to this in vivo average template in the BMA2.0 space. Next, we took all the transformed in vivo brains, flipped them along the sagittal axis, and calculated the average to create our BMA2.0 in vivo average template.

Population-based marmoset brain atlas construction

To construct the population-based atlas, we first need to build the 10 individual atlases. To do this, we take the region label images in myelin image space, with intensities of the label map corresponding to a region number in our brain regions lookup table. We then applied the transforms from individual myelin to individual block face space to label map image, restoring them to the original brain shape. Next, we stacked the individual label map images into a 3D volume and then applied compound transforms to transform it first to its individual MRI space, then to the BMA2.0 average template space. This process is applied to all 10 individuals, giving us 10 individual brain atlases in BMA2.0 space.

All 10 individual atlases used for our population-based atlas construction in coronal, sagittal, and axial views are shown in Figure 5. All 10 atlases are transformed to the BMA2.0 average space from individual myelin space after reconstruction, transform order: individual myelin to individual block face, then to individual ex vivo T2 MRI, and finally to BMA2.0 ex vivo T2WI average template. Nearest neighbor interpolation is used when transforming labels. All 10 transformed atlases have a resolution of $300 \times 360 \times 220$ pixels, and with a voxel size of $100\mu m \times 100\mu m \times 100\mu m$.

For our new BMA2.0 population-based atlas, we want to make the region labels truly symmetrical to accompany our new population average template. This also simplifies the atlas construction process as we need to construct the atlas for the left hemisphere only, and then mirror it to the right hemisphere along the sagittal axis. But this does not exclude the right hemisphere data of the 10 individual atlases during construction. We also account for the right hemisphere data by flipping the 10 individual atlases along the sagittal axis to obtain 20 atlases in total. Thus, both the left and right hemisphere label data will be used during the single hemisphere atlas construction.

Streamline-based label assignment

To calculate the average label in the BMA2.0 space using the 10 individual atlases, we used the Laplacian technique with two boundaries introduced by Jones et al.[35] and used by Majka et al.[20], based on a streamline-based method to assign the most probable label per streamline. The Laplace equation is the following:

$$\nabla^2 f = \frac{\partial^2 f}{\partial x^2} + \frac{\partial^2 f}{\partial y^2} + \frac{\partial^2 f}{\partial z^2} = 0$$

To compute the required Laplacian for the streamline-based method, we first need to distinguish several areas within the data to begin the calculation, such as the cortical mask, background, and inner-cortical surface segmentation.

For cortical mask and background segmentation, we used transforms from BMA2019 to BMA2.0 to transform the existing cortical mask and background segmentation for BMA2019 to BMA2.0. We then used 3D Slicer to make adjustments to the cortical mask in difficult areas such as the gap in the lateral sulcus. We then manually defined the inner-cortical surface within

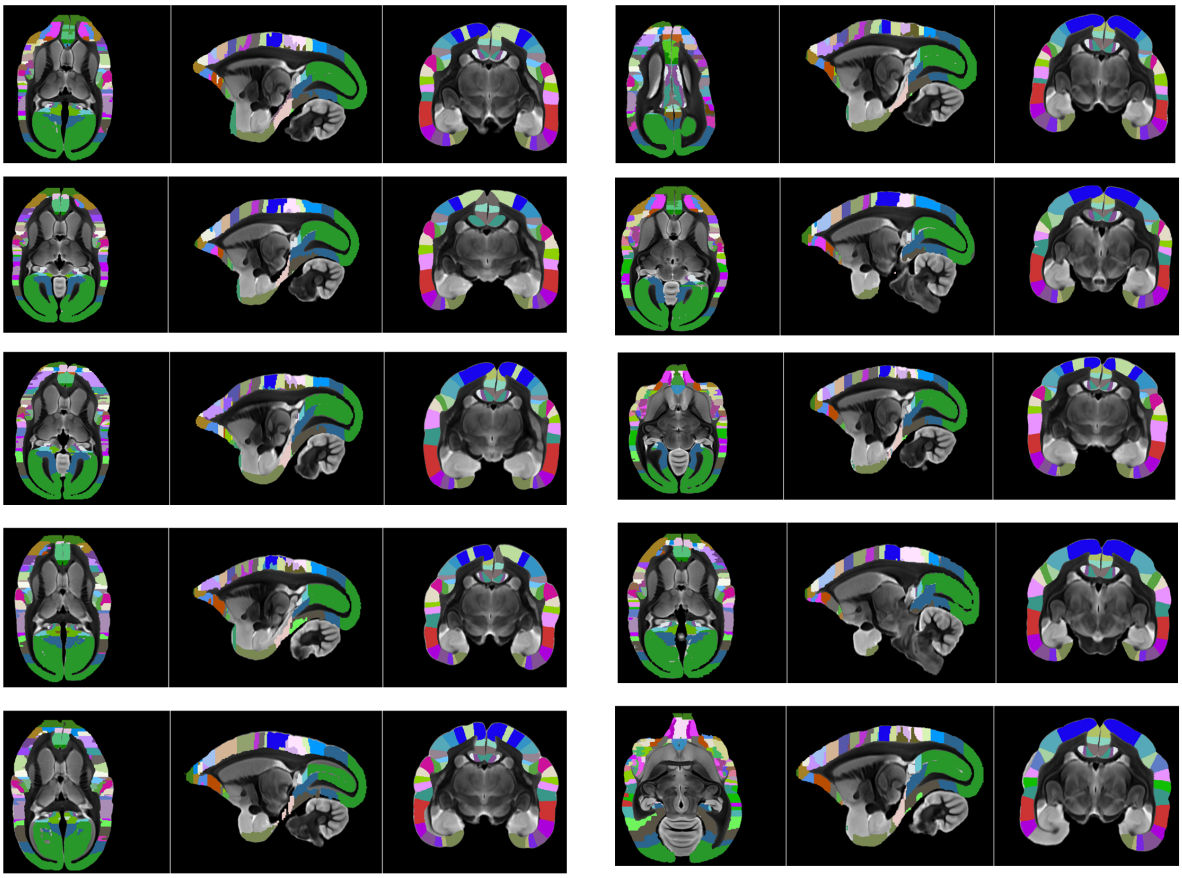

Figure 5. Axial, sagittal, and coronal views of the 10 individual cortical atlases in its individual space overlay onto its individual ex vivo T2WI MRI that are used for our BMA2.0 population-based atlas construction, where each individual atlas were reconstructed using out NanoZoomer pipeline. It also demonstrated individual atlas variability, highlighting the disadvantage of a single brain atlas. It also shows the disadvantage of brain annotation using coronal sections in the sagittal view, where the cortical region boundaries does not follow cortical columnar anisotropy (direction normal to cortical layers).

the cortical mask for BMA2.0. The cortical mask and background segmentation information were used to delineate the outer surface of the cerebral cortex. This was achieved by examining the overlap between the outer surface of the cortical mask and the background, excluding the inner surface.

Once we have defined the outer and inner surfaces, we can use them for the Laplace calculation within the cortical mask. Here, we defined $f = 1$ for the inner surface and $f = 2$ for the outer surface, we then compute the Laplace to get a smooth transition from the inner surface to the outer surface within the cortical mask of the whole 3D volume, where each voxel represents a gradient $\nabla(x, y, z)$.

Next, for the streamlined calculation, we chose to utilize the mid-surface for generating starting points. To do this, we first take the mid-surface in our BMA2019 flat map package and apply transforms from BMA2019 to BMA2.0 to transform all vertices on the mid-surface to BMA2.0 space. We then select points on this new mid-surface that intersect the cerebral cortex mask to provide us with the starting points for the streamline calculation. We also generated an additional 4 random points per starting point to expand the number of streamlines generated during the calculation to ensure streamlines extend to all points within the cerebral cortex.

To calculate the label assignment for each streamline along the mid-surface points, the following procedure is undertaken. Initially, all 20 atlases are loaded (10 original and 10 flipped). The initial positions for each streamline were generated by first identifying the vertices of the mid-cortical surface, defined by the coordinates (x, y, z), and then verifying the overlap of each vertex with the cortical mask. These vertices were later incorporated into the list of initial locations. Four random points were generated and added to the list, increasing the total number of starting points to 1,336,640. Next, the calculated Laplace volume was converted into gradients, giving us directions to follow in 3D for each point. The streamline calculation was initiated from each point in the list, resulting in the calculation of two streamlines. These streamlines followed the gradients towards the inner

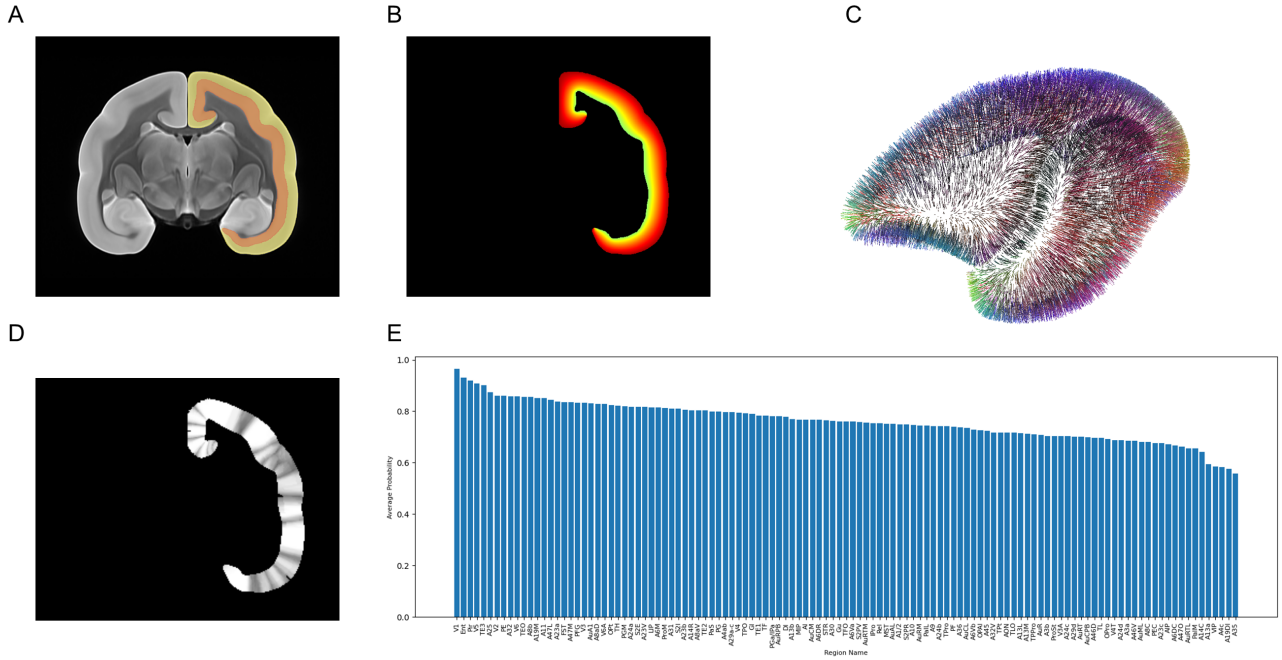

Figure 6. Streamline based label assignment using Laplace volume (A) manual segmentation of cerebral cortex (yellow) and mid-cortical surface (orange) based on BMA2.0 average template. (B) An example of a single coronal slice of the Laplace volume calculated using the information from manual segmentation, starting from the inner white matter surface (yellow) toward the outer pial surface (orange). (C) 3D visualization of streamlines generated from mid-cortical surface toward outer pial surface, to verify that the generated streamlines follow the correct direction from Laplace. (D) visualization of label assignment probabilities within the cerebral cortex after streamline calculations, with lighter gray indicating higher probability and darker gray indicating lower probability. (E) graph of average label assignment probabilities per label, sorted from highest to lowest probability.

and outer surfaces of the cerebral cortex. At each step, label assignments were collected from all 20 atlases along the streamline until it reached the inner or outer surface. Finally, the label with the highest probability along the streamlines was selected and assigned to all points along the inner and outer streamlines.

Integration of Subcortical Structures

The subcortical regions for our population-based atlas were added from a previous release (BMA2017), where the subcortical regions were delineated by Hashikawa et al.[16] based on a single brain. Due to the difficulties of identifying subcortical regions compared to cortical regions, we could not do this for all 10 individuals in a reasonable time frame. For image registration, the BMA2017 Nissl brain was initially registered to the BMA2.0 average Nissl template, incorporating MRI contrast as a constraint, as the regions were identified using Nissl contrast in BMA2017. Next, we used the transforms from registration results to transform the BMA2017 labels into the BMA2.0 space. We then used the cortical mask to exclude the cortical regions and added the remaining subcortical regions into our BMA2.0 atlas.

After mapping BMA2017 subcortical regions to BMA2.0, a large number of subcortical region labels were manually edited to improve the alignment to our population average template using 3D Slicer. We first identify regions with bad alignments by eye. Subcortical regions with bad alignments are then isolated based on their region label numbers. These regions were then manually edited slice by slice across the entire brain, where we used all 3 contrasts (MRI, myelin, and Nissl) with the original BMA2017 serving as a reference, to guide our manual segmentation, as some subcortical region borders can only be identified in one contrast. After each region edit, we inspect them in all 3 views (axial, coronal, and sagittal) and apply smoothing to ensure the smoothness in 3D.

Comparing to the original BMA2017 subcortical atlas, we had to combine the sub regions within the inferior olive (IC), namely, Inferior olive; dorsal nucleus (IOD) and Inferior olive; principal nucleus (IOPr) as we can not delineate the correct boundaries for those regions using the average templates we have. At the end, we manually rectified 50 badly aligned subcortical regions after image registration.

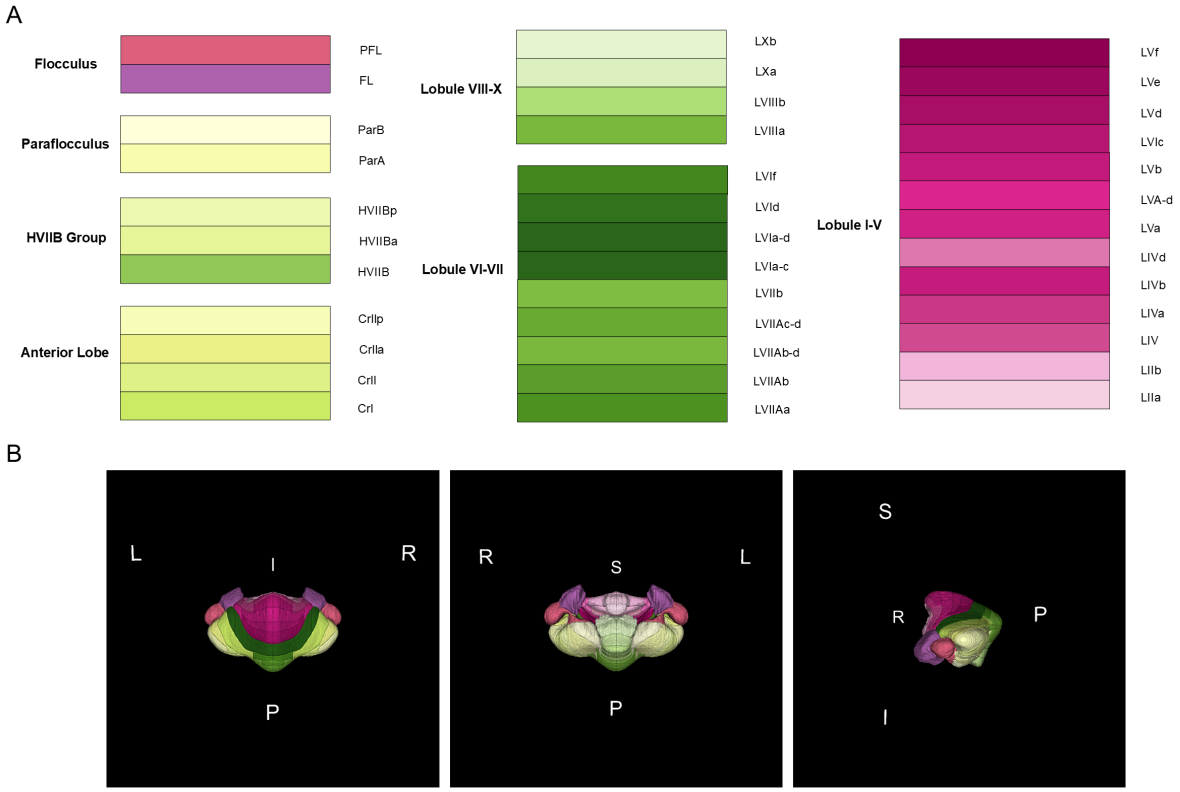

Figure 7. Overview of the cerebellum atlas. (A) Color coding table of the cerebellum atlas by Lin et al., with region groups representing main brain function. (B) 3D reconstruction of the cerebellum atlas in superior, inferior and left hemisphere views.

Cerebellar Lobule Delineation

To achieve accurate anatomical delineation of the cerebellum for the BMA2.0, we manually segmented each lobule, resulting in the identification of 45 distinct cerebellar cortical regions and refined 4 deep cerebellar nuclei (DCN). Each cerebellar lobule was annotated in the sagittal plane, which provided optimal visualization of lobular boundaries, while the DCN were delineated in the coronal plane to maximize clarity of internal nuclear structures.

These structures were manually annotated using high-resolution (40 µm) T2WI ex vivo MRI in conjunction with corresponding Nissl-stained histological sections. The delineation process was cross-validated with the reference atlas provided by Lin et al.[36], both through online access and in-person consultation.

To ensure accurate boundary demarcation between the white matter and the granular layer (GL), we additionally performed manual segmentation of the arbor vitae. This characteristic, tree-like branching structure of the cerebellar white matter was essential for precisely refining lobular borders within the BMA2.0 ex vivo T2WI population-average template.

We refined the cerebellar lobule definitions by comparison with the Lin et al.[36] reference, ultimately establishing a total of 45 cerebellar regions per hemisphere. The incorporation of this detailed cerebellar atlas significantly enhances the anatomical completeness of BMA2.0, supporting comprehensive studies of whole-brain functional networks, structural connectivity, and regional integration across the marmoset brain.

Flat map and cortical surfaces

For the flat map and cortical surfaces, we used transforms from BMA2019 to BMA2.0 to transform the vertex coordinates of the mid-cortical surface from BMA2019 space to BMA2.0 space, giving us a mid-cortical surface in BMA2.0 shape. We then used the command line program (wb_command -volume-to-surface-mapping) from Connectome Workbench[37] to map the BMA2.0 atlas to this transformed mid-cortical surface, giving us region labels to coordinate mapping for the flat map, the resulting surfaces and flat map are shown in Figure 1D.

Interoperability

In this section, we describe the interoperability of our BMA2.0 atlas to other existing atlases.

Backward compatibility to BMA2017 and BMA2019

In our BMA2.0 package, we have included both forward and backward transforms to our previous releases, BMA2017 and BMA2019. For BMA2017, we have used cortical and background segmentation as constraints to register between the BMA2017 T2WI MRI and the BMA2.0 T2WI average template. Similarly, segmentation constraints were used to register between the BMA2019 T2WI average template and the BMA2.0 T2WI average template, as registration between similar modalities is more accurate.

Those transforms can be used to transfer any data that was registered or analyzed in BMA2017 or BMA2019 to our new BMA2.0 space. It can also be used to transform data that was mapped to the BMA2019 mid-cortical surface/flat map to the BMA2.0 ones as well.

Transforms to other standard templates

To further expand the interoperability of BMA2.0, we also provide transformations to other widely used marmoset brain atlases, such as the Marmoset Brain Mapping Atlas Version 2 (MBMv2)[38] and the Marmoset Brain Connectivity Atlas (MBC)[39]. These transformations enable users to map data between BMA2.0 and those spaces, such as white matter pathways from MBMv2 or tracer projections from Marmoset Brain Connectivity Atlas. This interoperability allows comparative studies and integration of datasets generated using different reference frameworks, enhancing the accessibility of BMA2.0 for previous studies.

Data Records

The BMA2.0 dataset is separated into 3 parts, the main atlas part of the dataset includes several volumetric files in compressed NIfTI format (.nii.gz), containing the atlas, and multi-modal templates. The corresponding region names, and color lookup table is provided in text format (.ctbl). Next, the flat map part of the dataset includes the flat map, region labels and cortical surfaces (outer, mid and inner) in GIfTI format (.gii). Description of the atlas, templates and flat map files are given in Table 3.

Lastly, the transformations part of the dataset include direct and inverse warp fields in compressed NIfTI format (.nii.gz) and affine transforms (.mat), providing transforms between BMA2.0 and other template spaces (BMA2017[14], BMA2019[15], MBMv2[38], and MBC[39]). Description of the transformation files are given in Table 4.

Filename	File type	Description
BMAv2_atlas.nii.gz	NIfTI	BMA2.0 atlas with population-based cortical parcellations
BMAv2_avg_exvivo_T2WI.nii.gz	NIfTI	Population average ex vivo T2WI MRI template (n=91)
BMAv2_avg_Myelin.nii.gz	NIfTI	Population average myelin contrast template (n=10)
BMAv2_avg_Nissl.nii.gz	NIfTI	Population average Nissl contrast template (n=10)
BMAv2_avg_invivo_T2WI.nii.gz	NIfTI	Population average in vivo T2WI MRI template (n=446)
BMAv2_atlas_labels.ctbl	Text	Region and color lookup table for BMA2.0 atlas
BMAv2_Scene.mrml	XML	3D Slicer scene file for BMA2.0 atlas and templates
BMAv2.lh.flatmap.surf.gii	GIfTI	BMA2.0 left hemisphere cortical flat map
BMAv2.lh.pial.surf.gii	GIfTI	BMA2.0 left hemisphere pial surface
BMAv2.lh.graymid.surf.gii	GIfTI	BMA2.0 left hemisphere mid-cortical surface
BMAv2.lh.white.surf.gii	GIfTI	BMA2.0 left hemisphere white matter surface
BMAv2.lh.regions.label.gii	GIfTI	BMA2.0 left hemisphere region labels for flat map and cortical surfaces
BMAv2_flatmap_package.scene	XML	Connectome workbench scene file for loading BMA2.0 flat map package

Table 3. Data records of BMA2.0 atlas, templates and flat map.

The BMA2.0 atlas delineates a total of 323 regions per hemisphere, that includes population-based cerebral cortex delineation (n=10) of 117 regions, subcortical delineation of 156 regions, and cerebellar lobule delineation of 45 regions.

The region name and color lookup table for cerebral cortex and subcortical areas were adopted from BMA2017[14], which was first defined by Iriki et al.[17]. We have extended the list by adding 45 cerebellar lobule delineation per hemisphere (region ID 787-831 on the right hemisphere and 10787-10831 on the left hemisphere), region name and color was defined by Lin et al.[36] based on main brain function as shown in Figure. 7A.

Technical Validation

In this section, we examine the confidence of region label assignment using streamline-based method, and various pilot studies based on the BMA2.0 templates.

Filename	File type	Description
BMA2017_to_BMAv2_1Warp.nii.gz	NIfTI	Warp field from BMA2017 to BMA2.0
BMA2017_to_BMAv2_1InverseWarp.nii.gz	NIfTI	Warp field from BMA2.0 to BMA2017
BMA2017_to_BMAv2_0GenericAffine.mat	MATLAB data	Affine transforms from BMA2017 to BMA2.0
BMA2019_to_BMAv2_1Warp.nii.gz	NIfTI	Warp field from BMA2019 to BMA2.0
BMA2019_to_BMAv2_1InverseWarp.nii.gz	NIfTI	Warp field from BMA2.0 to BMA2019
BMA2019_to_BMAv2_0GenericAffine.mat	MATLAB data	Affine transforms from BMA2019 to BMA2.0
MBMv2_to_BMAv2_1Warp.nii.gz	NIfTI	Warp field from MBMv2 to BMA2.0
MBMv2_to_BMAv2_1InverseWarp.nii.gz	NIfTI	Warp field from BMA2.0 to MBMv2
MBMv2_to_BMAv2_0GenericAffine.mat	MATLAB data	Affine transforms from MBMv2 to BMA2.0
MBC_to_BMAv2_1Warp.nii.gz	NIfTI	Warp field from MBC to BMA2.0
MBC_to_BMAv2_1InverseWarp.nii.gz	NIfTI	Warp field from BMA2.0 to MBC
MBC_to_BMAv2_0GenericAffine.mat	MATLAB data	Affine transforms from MBC to BMA2.0

Table 4. Data records of transformations (affine and warp fields) between BMA2.0 and other templates.

Confidence of streamline-based label assignment

During the streamline calculation, at the same time, we also collected data to calculate the confidence of the label assignments. An example of the results in coronal view is shown in Figure 6D, where gray scale values are used to visualize the confidence of label assignments, with darker shades of gray indicating lower confidence and lighter shades of gray indicating higher confidence.

A more detailed analysis of the average label assignment confidence is shown in Figure 6E, showing the average confidence of label assignments for each cortical region. Here, we were expecting the confidence to be low for regions around the lateral sulcus, due to the difficulty of image registration for for that area, but we were surprised to find out that the bottom 5 regions with the lowest confidence are Area 35 of cortex (A35), Area 19 of cortex; dorsointermediate part (A19DI), Area 4 of cortex; part c (A4c), Ventral intraparietal area of cortex (VIP), and Area 13a of cortex (A13a) were the smaller regions that are not around the lateral sulcus. This can be attributed to more overlap with the surrounding larger regions.

Population-Based DWI Calculation using In vivo Average Template

To demonstrate one use case of our BMA2.0 in vivo population template, we have taken the in vivo Diffusion-weighted imaging (DWI) data from the NA216 data set (N=126), where each data set contains 96 channels, to calculate a population average DWI and then perform fiber tracking and generate a population-based connectome of the common marmoset brain.

We first separate all 96 channels of each data set into individual NifTI files (12096 files in total), channel 1 of each data set is then registered to the BMA2.0 in vivo average template using ANTs. The resulting transform files for each brain are then used to transform all 96 channels of the individual dataset to the BMA2.0 average space. Averaging is then calculated for each of the 96 channels, with 126 datasets per channel. The 96 averaged channels are reconstructed back into a single NifTI file, giving us the population average DWI.

The fiber tracking is then performed using DSI-studio's [4] tractography tool[40–43] using the calculated population average DWI, 5,000,000 tracks were generated, and the fiber tracking result is shown in the left image in Figure 8A, B. The average tract length is 24.75 mm in our result, which is consistent with another marmoset DWI tractography study by Schaeffer et. al[44].

The fiber tracking result visualized in diffusion space is shown in Figure 8C, which is overlayed with the BMA2.0 in vivo average template. Our BMA2.0 atlas is then used to generate brain regions (N=636) as region of interests (ROI) and they are all mapped to the tractography result using DSI-studio, shown in the right image in Figure 8A, the population average connectome of the marmoset brain is then calculated using this information, and the result is shown in Figure 8C, which shows the strength of connection between all brain regions.

Validation of the Connectivity Matrix using Tracer Injection Dataset

To assess the anatomical validity of the BMA2.0 diffusion-based connectivity matrix, we compared it with the axonal tracer-based interareal connectivity matrix reported by Majka et al.[39], which is one of the most comprehensive mesoscale connection maps available for the marmoset cortex.

Despite being derived from entirely separate individuals, using different methodologies (in vivo DWI vs. retrograde tracer injections) shown in Figure 9C, we observed a substantial correlation (Pearson's r = 0.4605) between the diffusion tractography-based and tracer-based area-to-area connectivity weights. This degree of correspondence is comparable to previous

[4] https://dsi-studio.labsolver.org/

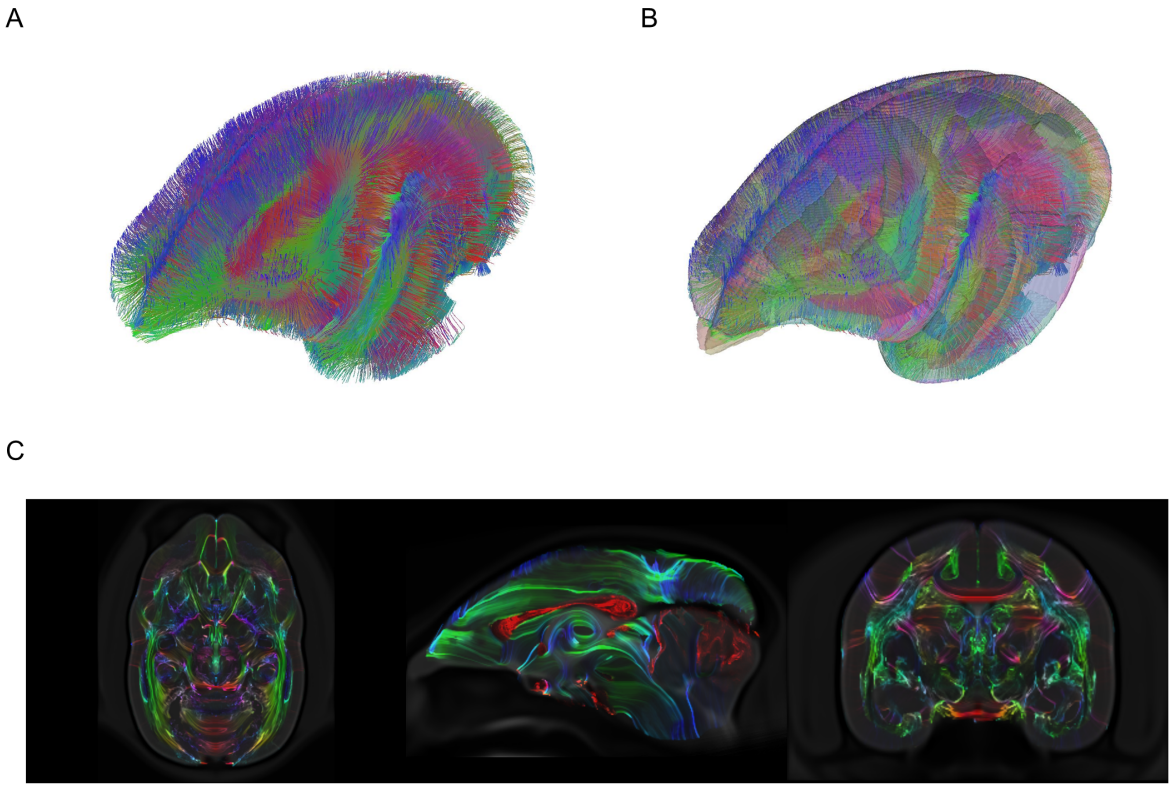

Figure 8. Population-based tractography calculated using the BMA2.0 in vivo average template. (A) Visualation of fiber tracking (dsi studio) using the population average in vivo diffusion MRI data (N=126). (B) Fiber tracking result and with BMA2.0 whole brain regions overlay (ROI=636). (C) Axial, sagittal, and coronal views of fiber tracking density visualized in diffusion space overlayed onto BMA2.0 in vivo average template.

large-scale cross-modal studies in mice, such as the Allen Mouse Brain Connectivity Atlas (Spearman r $\approx$ 0.46 for area-level comparisons), and underscores the utility of the BMA2.0 connectome for network-level analyses.

In contrast to mice, such systematic comparisons between tracer and tractography data across the entire cortex have been rare in macaques. One landmark study using the same individual macaque for both tracer injections and postmortem DWI reported higher correlation ($r \approx 0.56$) under idealized conditions (Donahue et al.[45]), but such designs are logistically constrained and not generalizable. Our cross-individual result ($r = 0.4605$) thus demonstrates a high degree of robustness and validates the anatomical relevance of our connectome under realistic application conditions.

Given the challenging nature of intermodal normalization, especially in primates where individual anatomical variation is high, this level of agreement highlights the potential of BMA2.0 to serve as a common coordinate framework for integrative studies. We expect that such validated connectomic maps will enhance downstream analyses, including computational modeling, cross-species comparisons, and integration with functional and genetic data.

Estimation of Layer 1-3 Thickness Using Myelin Contrast

To quantify the thickness of supragranular layers (layers 1-3) across the marmoset neocortex, we used the population average myelin-stained volume from the BMA2.0 atlas. Myelin staining exhibits a robust laminar contrast in the form of a prominent "middle band," which corresponds approximately to the layer 3-4 boundary. Compared to Nissl staining, which requires high-magnification inspection and is less reliable at lower resolution due to variability in cell density and staining intensity, this feature provides a more consistent and reproducible laminar landmark across regions and individuals.

The upper boundary of the middle band was manually traced by a well-trained neuroanatomist (N.I.) based on histological expertise. For each cortical location, the distance from the pial surface to the traced upper edge of the middle band was computed using a Laplacian streamline coordinate system defined between the pial and white matter surfaces. The resulting measurement was used as a proxy for the combined thickness of layers 1-3.

In parallel, the lower boundary of the middle band was also traced for each area. While its interpretation varies across regions—sometimes aligning with the layer 4-5 boundary in granular areas, or existing without clear cytoarchitectonic

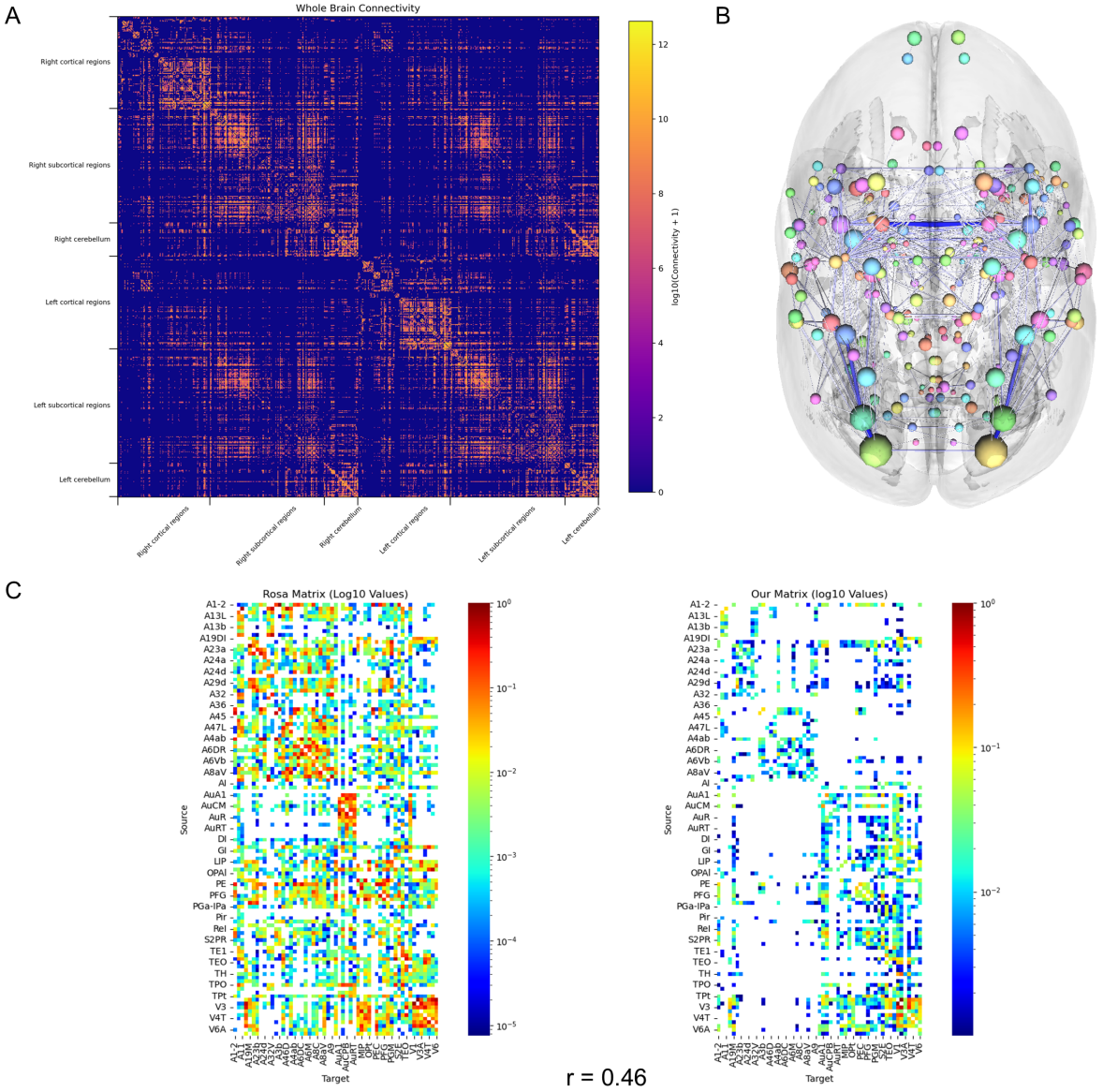

Figure 9. Analysis of the connectivity matrix generated from tractography. (A) Whole brain connectivity matrix (ROI=636) generated from fiber tracking result based on in vivo population average DWI data. (B) 3D visualization of the connectivity matrix in axial view, showing strong connections between posterior visual regions. (C) Comparison of connectivity matrix between the marmoset brain connectivity atlas project, and ours, using the same ROIs and region orders. The Pearson correlation score between to the two matrices is 0.46.

counterparts in agranular regions—it is displayed in figures (Figure. 10A) as a reference only, not used for quantification.

These thickness values were projected onto the 2D flatmap representation of the BMA2.0 atlas to visualize spatial distributions. The resulting maps revealed systematic gradients along dorsal-ventral and anterior-posterior axes, consistent with previously described anatomical and functional hierarchies in the primate cortex (Figure. 10B, C).

Per-Area Intensity Profiling and Data Availability

To support reproducibility and enable region-wise comparisons, we performed a per-area analysis of cortical laminar profiles based on Nissl staining. For each cortical area defined in the BMA2.0 parcellation (e.g., TE2, V1, A1/2), we extracted normalized intensity profiles along the pia-white matter axis and recorded the depth of the manually annotated upper edge of the myelin-defined middle band.

In addition to the flatmap-based visualizations, we provide the following data per area:

- Nissl intensity profiles across normalized cortical depth.
- Depth of the middle band upper border (used for estimating layers 1-3 thickness).
- (For reference only) Depth of the lower border of the middle band, displayed in figures as a visual guide.

All relevant data—including per-area intensity traces, middle band annotations, and summary thickness values—are available at [data repository URL]. The repository also includes the Python scripts used for analysis and visualization. Access is provided to reviewers via a private link, and the dataset will be released under a public DOI upon publication.

Regional variation in supragranular layer thickness and system-level gradients

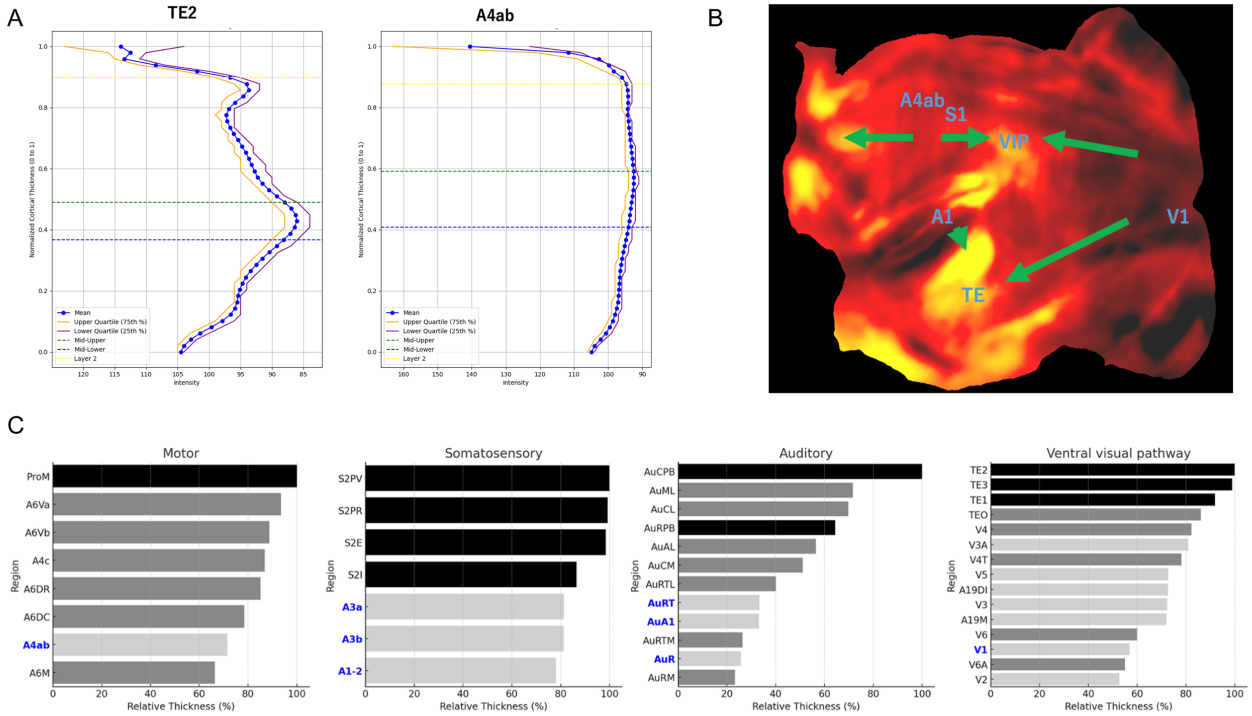

Figure 10. Regional gradients and cytoarchitectonic features of supragranular (layer 1-3) thickness across the marmoset cortex. (A) Nissl intensity profiles along normalized cortical depth (from pial = 0 to white matter = 1) for two representative areas: TE2 (temporal association cortex) and A4ab (primary motor cortex). TE2 shows a prominent middle-band-associated peak, aligned with a dense Nissl profile at mid-depth. In contrast, A4ab—an granular area—shows a flat Nissl profile with no clear middle band, consistent with its lack of layer 4. (B) Thickness of supragranular layers (L1-3) across the neocortex, computed as the distance from the pial surface to the upper edge of the myelin-defined middle band. Values are projected onto the BMA2.0 flatmap. Warmer colors indicate greater thickness. Arrows highlight example regions from different cortical systems. Arrows indicate presumed hierarchical progression within each cortical system (motor, somatosensory, auditory, and visual), anticipating the quantitative gradients shown in Panel C. (C) Bar plots showing normalized supragranular (L1-3) thickness across four cortical systems. Motor system: primary motor cortex (A4ab) →premotor areas (A6) →promotor (ProM). Somatosensory system: primary somatosensory areas (A3a, A3b, A1/2) →secondary somatosensory areas (S2). Auditory system: core regions (AuA1, AuR, AuRT) →belt and parabelt regions. Ventral visual stream: V1 →V2-V4 →inferotemporal areas (TE). Within each system, L1-3 thickness increases along presumed cortical hierarchies, supporting the idea that supragranular expansion correlates with integrative processing demands. Gray scale indicates hierarchical level (black: higher, dark gray: middle, light gray: lower), and primary areas are highlighted in blue.

To examine the laminar organization across cortical areas, we quantified the thickness of supragranular layers (layers 1-3) using the population average myelin-stained template from the BMA2.0 atlas. The upper boundary of the middle band—visually prominent in myelin staining and approximating the border between layers 3 and 4—was manually traced by an experienced neuroanatomist for each area. Using a Laplacian streamline coordinate system from the pial surface to white matter, we measured the distance to the traced boundary, which served as a proxy for layer 1-3 thickness.

The resulting measurements were projected onto the 2D cortical flatmap (Figure 10A), revealing systematic gradients across the cortical sheet. Association areas such as TE and ProM exhibited the greatest supragranular thickness, whereas motor areas and medial wall regions (e.g., A4ab, A6M) showed consistently thinner upper layers.

To interpret these patterns in relation to underlying cytoarchitecture, we extracted Nissl intensity profiles across normalized cortical depth for representative areas. In TE2, a distinct contrast corresponding to the middle band was observed, whereas in A4ab, the middle band was weak or absent (Figure 10B). This finding is consistent with the classical notion that A4ab is an agranular region, lacking a well-defined layer 4. Moreover, in TE2, the Nissl density peak corresponded closely with the location of the myelin-defined middle band, suggesting that in this region, the middle band reflects the anatomical position of layer 4.

We further compared supragranular thickness across major functional systems using representative regions (Figure 10C). In the motor-frontal system, a rostro-caudal gradient was observed, with ProM and A6Va exhibiting thicker upper layers than A4ab. In the somatosensory system, secondary and belt areas such as S2PV and S2PR had greater L1-3 thickness than primary sensory areas like A1/2. The auditory system showed increasing supragranular thickness from core to belt and parabelt regions. Similarly, in the ventral visual stream, TE2 showed the greatest L1-3 thickness, with a progressive reduction toward V1.

These results suggest that supragranular laminar expansion is a structural correlate of cortical hierarchy and may serve as a meaningful morphological feature associated with information integration across cortical systems.

Discussion

The population average histological and MRI templates presented in the BMA2.0 atlas not only serve as a standardized spatial framework for multi-modal data integration, but also enable novel morphometric analyses based on laminar features. In this study, we focused on quantifying the thickness of supragranular layers (layers 1-3) across the cortex using the upper boundary of the myelin-defined middle band as a structural landmark.

The resulting thickness map revealed systematic spatial gradients across dorsal-ventral and anterior-posterior cortical axes (Figure 10A), consistent with established principles of functional and anatomical hierarchies in the primate cortex. Importantly, this laminar measurement approach is feasible even at moderate resolution and is robust across cortical regions, in contrast to Nissl-based laminar delineation, which often requires high-magnification microscopy and is sensitive to staining variability.

To further validate this interpretation, we analyzed representative Nissl intensity profiles (Figure 10A). In TE2, a distinct peak in Nissl density corresponded closely to the location of the myelin middle band, suggesting correspondence with a well-developed layer 4. In contrast, A4ab—a classically agranular region—showed neither a clear middle band nor a distinct Nissl-defined peak, supporting the notion that myelin band contrast reflects underlying laminar architecture in a region-specific manner.

Comparative analysis across cortical systems (Figure 10B, C) demonstrated that supragranular thickness increases systematically along putative processing hierarchies—for example, from V1 to TE2 in the ventral visual stream, and from primary to higher regions in the motor, somatosensory and auditory cortices (Figure 10B, C). These findings support the idea that supragranular expansion is a structural correlate of integrative processing and cortical complexity.

Taken together, these results demonstrate that the BMA2.0 atlas provides not only an anatomical coordinate framework but also a morphometric substrate for studying cortical microstructure. This approach may further facilitate future efforts to build probabilistic laminar maps across individuals and species, analogous to developments in rodent and human brain mapping.

Functional dynamics comparison by MTESS

In this section, we investigated whether anatomical segmentation (BMA2.0) captures functional activity. To do this, we used awake resting-state (rs-) fMRI data from four marmosets[46,47] and quantified the similarity of multivariate time-series across 12 sessions within each individual using Multivariate Time-series Ensemble Similarity Score (MTESS)[48]. We hypothesized that if the region segmentation adequately captures functional activity, the similarity of multivariate time-series within an individual would be higher than that of non-functional segmentation. Transforming the BMA2.0 atlas into the rs-fMRI image space resulted in 544 ROIs (Figure 11A top). In addition, K-means clustering was performed based on voxel distance to divide the marmoset brain into 544 regions, which was named DistKm (Figure 11A bottom). DistKm does not follow anatomical regional division at all, and by comparing the similarity of the within-individual multivariate time-series in the ROI types of BMA2.0 and DistKm, it is possible to test whether anatomical regional division has no functional meaning (null hypothesis). We calculated the MTESS for each session (resulting in a 48×48 matrix) for the four marmosets (Figure 11B), extracted within-individual session comparisons, and compared BMA2.0 with DistKm (Figure 11C). The results showed that BMA2.0 had significantly higher similarity, better capturing functional activity, suggesting that anatomical segmentation has functional meaning.

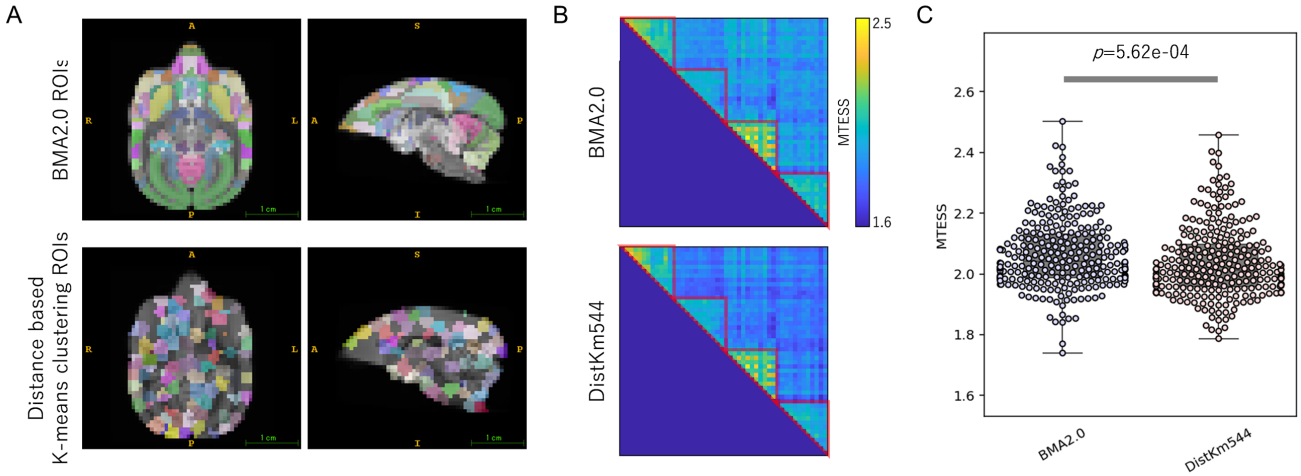

Figure 11. Comparing multivariate time-series similarity between BMA2.0 and distance based K-means clustering ROIs. (A) Example horizontal (z=22/45) and sagittal (x=22/45) planes in each ROI type. (top) BMA2.0 atlas ROIs. (bottom) distance based K-means (DistKm) clustering ROIs. (B) MTESS matrix results of BMA2.0 ROIs (top) and DistKm ROIs (bottom). Similarity of rs-fMRI multivariate time-series of 4 animals x 12 sessions (48 sessions in total). The higher the value, the higher the similarity of multivariate time series between sessions. Red triangles indicate inter-session similarity for each individual. (C) Similarity between individual sessions for each ROI type (red triangles in B); BMA2.0 atlas is significantly higher than DistKm ROIs (p=5.62e-04, Mann-Whitney U test).

Usage Notes

All NIfTI data provided in the BMA 2.0 atlas package are compatible with a wide range of neuroinformatics and image analysis software. These files can be loaded using software such as 3D Slicer[31] (version 5.6.2) and ITK-SNAP[49] (version 4.0.2), allowing users to inspect and explore BMA2.0 templates alongside the atlas. We have provided a 3D Slicer scene file (.mrml) that the user can open which loads all the templates, region labels and region definitions of BMA2.0.

We recommend using Python for code-based processing of NIfTI files for BMA2.0. Python libraries such as Nibabel[50] (version 5.3.2) and SimpleITK[51] (version 2.5.0) provide access to both voxel data and metadata, that contain information on resolution, voxel spacing, orientation, etc.

Registration to our multimodal templates can be done using ANTs command line interface, tutorial on how to perform image registration and apply transforms using ANTs can be found in the Brain/MINDS data portal [5]. For interpolations, users should use "NearestNeighbor" when transforming labels and "Linear" for templates.

For users who prefer working with Python, we recommend using the ANTsPy[25] library, which is the Python interface to ANTs that provides equivalent functionality such as reading NIfTI files, running image registration, and applying transformations.

The flat map and cortical surfaces can be loaded and visualized using Connectome Workbench[37]. We provide a scene file (.scene) for Connectome Workbench that will load the flat map, cortical surfaces and labels. For users that would like to access flat map and surface data using Python, we recommend using the Nibabel[50] (version 5.3.2) library.

Data Availability

The BMA2.0 atlas package including the atlas, multi-modal templates, cortical flat map and surfaces, forward and backward transforms to other atlas is public available on figshare: https://doi.org/10.6084/m9.figshare.29992687.

Code availability

For our BMA2.0, image data processing and atlas construction relied on a combination of custom Python scripts for small tasks and extensive manual processing. These scripts are not sufficiently documented for general use and are therefore not publicly released. All data processing can be reproduced by following the procedures and software packages described in the Methods section. Additional details about the atlas, and templates construction can be provided by contacting the corresponding author.

[5] https://dataportal.brainminds.jp/ants-tutorial

Acknowledgements

This research was supported by Japan Agency for Medical Research and Development (AMED) under Grant Numbers JP15dm0207001 and JP23wm0625001. This work was supported by JSPS KAKENHI under Grant Numbers JP22H05163 and 24K03256 to K.N. This research was supported by Japan Agency for Medical Research and Development (AMED) under Grant Numbers: JP19dm0207088, JP24wm0625414, and JP24wm0625404 to K.N

Author contributions statement

R.G and A.W performed all the data processing to construct the atlases, multi-modal templates, transforms data, flat map and its corresponding surfaces. N.I, H.A and T.T collected the raw data, performed histological staining, and delineated cortical regions. K.N provided region segmentation data for T2WI MRI data. J.H provied MRI data for in vivo and ex vivo template construction. R.G, K.N, S.H and J.W edited subcortical regions suprivised by N.I. M.L performed cerebellar lobule delineation. R.G and N.I analysed DWI-based tractography and estimation of layer 1-3 thickness using myelin contrast. T.O performed functional dynamics comparison by MTESS. S.I, P.D, T.Y, and H.O and contributed to the review and editing of the manuscript. All authors reviewed the manuscript.

Competing interests

The authors declare that they have no known competing financial interests or personal relationships that could have appeared to influence the work reported in this manuscript.

References

1. Okano, H. *et al.* Brain/minds: A japanese national brain project for marmoset neuroscience. *Neuron* **92**, 582–590, 10.1016/j.neuron.2016.10.018 (2016).
2. Hardman, C. D. & Ashwell, K. W. S. *Stereotaxic and chemoarchitectural atlas of the brain of the common marmoset (Callithrix jacchus)* (CRC Press, Boca Raton, Fla, 2012), 1st ed. edn.
3. Kishi, N., Sato, K., Sasaki, E. & Okano, H. Common marmoset as a new model animal for neuroscience research and genome editing technology. *Dev. growth & differentiation* **56**, 53–62 (2014).
4. Worley, K. C. *et al.* The common marmoset genome provides insight into primate biology and evolution. *Nat. Genet.* **46**, 850–857, 10.1038/ng.3042 (2014).
5. King, A. The search for better animal models of alzheimer's disease. *Nature* **559**, S13–S13 (2018).
6. Philippens, I. H. *et al.* Acceleration of amyloidosis by inflammation in the amyloid-beta marmoset monkey model of alzheimer's disease. *J. Alzheimer's Dis.* **55**, 101–113 (2017).
7. Philippens, I. H. & Langermans, J. A. Preclinical marmoset model for targeting chronic inflammation as a strategy to prevent alzheimer's disease. *Vaccines* **9**, 388 (2021).
8. Rothwell, E. S. *et al.* The marmoset as an important primate model for longitudinal studies of neurocognitive aging. *Am. J. Primatol.* **83**, e23271 (2021).
9. Perez-Cruz, C. & de Dios Rodriguez-Callejas, J. The common marmoset as a model of neurodegeneration. *Trends Neurosci.* (2023).
10. Hearn, J. P., Abbott, D. H., Chambers, P. C., Hodges, J. K. & Lunn, S. F. Use of the common marmoset, Callithrix jacchus, in reproductive research. *Primates Med* **10**, 40–49 (1978).
11. Kurotaki, Y. & Sasaki, E. Practical Reproductive Techniques for the Common Marmoset. *J. Mammalian Ova Res.* **34**, 3 – 12, 10.1274/032.034.0103 (2017).
12. Paxinos, G., Watson, C., Petrides, M., Rosa, M. & Tokuno, H. *The marmoset brain in stereotaxic coordinates* (Elsevier Academic Press, 2012).
13. Nowinski, W. L. Usefulness of brain atlases in neuroradiology: Current status and future potential. *The Neuroradiol. J.* **29**, 260–268, 10.1177/1971400916648338 (2016). PMID: 27154190, https://doi.org/10.1177/1971400916648338.
14. Woodward, A. *et al.* The brain/minds 3d digital marmoset brain atlas. *Sci. Data* **5**, 180009, 10.1038/sdata.2018.9 (2018).
15. Woodward, A. *et al.* The nanozoomer artificial intelligence connectomics pipeline for tracer injection studies of the marmoset brain. *Brain Struct. Funct.* **225**, 1225–1243, 10.1007/s00429-020-02073-y (2020).

16. Hashikawa, T., Nakatomi, R. & Iriki, A. Current models of the marmoset brain. *Neurosci. research* **93**, 116–127 (2015).

17. Iriki, A., Okano, H. J., Sasaki, E. & Okano, H. *The 3-Dimensional Atlas of the Marmoset Brain: Reconstructible in Stereotaxic Coordinates* (Springer, 2018).

18. Watakabe, A. *et al.* Local and long-distance organization of prefrontal cortex circuits in the marmoset brain. *Neuron* **111**, 2258–2273 (2023).

19. Hata, J. *et al.* Multi-modal brain magnetic resonance imaging database covering marmosets with a wide age range. *Sci. Data* **10**, 221 (2023).

20. Majka, P. *et al.* Histology-based average template of the marmoset cortex with probabilistic localization of cytoarchitectural areas. *NeuroImage* **226**, 117625, 10.1016/j.neuroimage.2020.117625 (2021).

21. Liu, C. *et al.* Marmoset brain mapping v3: Population multi-modal standard volumetric and surface-based templates. *NeuroImage* **226**, 117620, 10.1016/j.neuroimage.2020.117620 (2021).

22. Liu, C. *et al.* A digital 3d atlas of the marmoset brain based on multi-modal mri. *NeuroImage* **169**, 106–116, 10.1016/j.neuroimage.2017.12.004 (2018).

23. Abe, H. *et al.* 3d reconstruction of brain section images for creating axonal projection maps in marmosets. *J. Neurosci. Methods* **286**, 102–113, 10.1016/j.jneumeth.2017.04.016 (2017).

24. Avants, B., Tustison, N. & Song, G. Advanced normalization tools (ants). *Insight J* **1–35**, 10.54294/uvnhin (2008).

25. Tustison, N. J. *et al.* The ANTsX ecosystem for quantitative biological and medical imaging. *Sci. Rep.* **11**, 9068 (2021).

26. Zhu, J.-Y., Park, T., Isola, P. & Efros, A. A. Unpaired image-to-image translation using cycle-consistent adversarial networks. In *Computer Vision (ICCV), 2017 IEEE International Conference on* (2017).

27. Shorten, C. & Khoshgoftaar, T. M. A survey on image data augmentation for deep learning. *J. Big Data* **6**, 60, 10.1186/s40537-019-0197-0 (2019).

28. Bloice, M. D., Roth, P. M. & Holzinger, A. Biomedical image augmentation using Augmentor. *Bioinformatics* **35**, 4522–4524, 10.1093/bioinformatics/btz259 (2019). https://academic.oup.com/bioinformatics/article-pdf/35/21/4522/30330763/btz259.pdf.

29. Avants, B. B. *et al.* A reproducible evaluation of ants similarity metric performance in brain image registration. *NeuroImage* **54**, 2033–2044, 10.1016/j.neuroimage.2010.09.025 (2011).

30. Isola, P., Zhu, J.-Y., Zhou, T. & Efros, A. A. Image-to-image translation with conditional adversarial networks. *CVPR* (2017).

31. Kikinis, R., Pieper, S. D. & Vosburgh, K. G. *3D Slicer: A Platform for Subject-Specific Image Analysis, Visualization, and Clinical Support*, 277–289 (Springer New York, New York, NY, 2014).

32. Belcher, A. M. *et al.* Large-scale brain networks in the awake, truly resting marmoset monkey. *J. Neurosci.* **33**, 16796–16804, 10.1523/JNEUROSCI.3146-13.2013 (2013). https://www.jneurosci.org/content/33/42/16796.full.pdf.

33. Schaeffer, D. J., Gilbert, K. M., Gati, J. S., Menon, R. S. & Everling, S. Intrinsic functional boundaries of lateral frontal cortex in the common marmoset monkey. *J. Neurosci.* **39**, 1020–1029, 10.1523/JNEUROSCI.2595-18.2018 (2019). https://www.jneurosci.org/content/39/6/1020.full.pdf.

34. Hori, Y., Cléry, J. C., Schaeffer, D. J., Menon, R. S. & Everling, S. Functional organization of frontoparietal cortex in the marmoset investigated with awake resting-state fmri. *Cereb. Cortex* **32**, 1965–1977, 10.1093/cercor/bhab328 (2021). https://academic.oup.com/cercor/article-pdf/32/9/1965/43401601/bhab328.pdf.

35. Jones, S. E., Buchbinder, B. R. & Aharon, I. Three-dimensional mapping of cortical thickness using laplace's equation. *Hum. brain mapping* **11**, 12–32 (2000).

36. Lin, M.-K. *et al.* An integrated mri-histology atlas of the marmoset cerebellum. https://www.marmosetbrainconnectome.org/cerebellum (2025). Accessed August 4, 2025.

37. Marcus, D. *et al.* Informatics and data mining tools and strategies for the human connectome project. *Front. Neuroinformatics* **Volume 5 - 2011**, 10.3389/fninf.2011.00004 (2011).

38. Liu, C. *et al.* A resource for the detailed 3D mapping of white matter pathways in the marmoset brain. *Nat. Neurosci.* **23**, 271–280 (2020).

39. Majka, P. *et al.* Open access resource for cellular-resolution analyses of corticocortical connectivity in the marmoset monkey. *Nat. Commun.* **11**, 1133 (2020).

40. Yeh, F.-C., Wedeen, V. J. & Tseng, W.-Y. I. Generalized q-sampling imaging. *IEEE Transactions on Med. Imaging* **29**, 1626–1635, 10.1109/TMI.2010.2045126 (2010).

41. Yeh, F.-C., Verstynen, T. D., Wang, Y., Fernández-Miranda, J. C. & Tseng, W.-Y. I. Deterministic diffusion fiber tracking improved by quantitative anisotropy. *PLOS ONE* **8**, null, 10.1371/journal.pone.0080713 (2013).

42. Yeh, F.-C., Liu, L., Hitchens, T. K. & Wu, Y. L. Mapping immune cell infiltration using restricted diffusion mri. *Magn. Reson. Medicine* **77**, 603–612, 10.1002/mrm.26143 (2017). https://onlinelibrary.wiley.com/doi/pdf/10.1002/mrm.26143.

43. Yeh, F.-C. Shape analysis of the human association pathways. *NeuroImage* **223**, 117329, https://doi.org/10.1016/j.neuroimage.2020.117329 (2020).

44. Schaeffer, D. J. *et al.* Diffusion-weighted tractography in the common marmoset monkey at 9.4t. *J. Neurophysiol.* **118**, 1344–1354 (2017).

45. Donahue, C. J. *et al.* Using diffusion tractography to predict cortical connection strength and distance: A quantitative comparison with tracers in the monkey. *J. Neurosci.* **36**, 6758–6770, 10.1523/JNEUROSCI.0493-16.2016 (2016). https://www.jneurosci.org/content/36/25/6758.full.pdf.

46. Okuno, T., Hata, J., Ichinohe, N. & Woodward, A. A reappraisal of the default mode and frontoparietal networks in the common marmoset brain. *Front. Neuroimaging* **2**, 1345643, 10.3389/fnimg.2023.1345643 (2024).

47. Okuno, T., Hata, J., Kawai, C., Okano, H. & Woodward, A. A novel directed seed-based connectivity analysis toolbox applied to human and marmoset resting-state fmri. *J. Neurosci.* **44**, e0389242024, 10.1523/JNEUROSCI.0389-24.2024 (2024).

48. Okuno, T. *et al.* Group surrogate data generating models and similarity quantifiation of multivariate time-series: A resting-state fmri study. *NeuroImage* **279**, 120329, 10.1016/j.neuroimage.2023.120329 (2023).

49. Yushkevich, P. A. *et al.* User-guided 3D active contour segmentation of anatomical structures: Significantly improved efficiency and reliability. *Neuroimage* **31**, 1116–1128 (2006).

50. Brett, M. *et al.* nipy/nibabel: 5.3.1, 10.5281/zenodo.13936989 (2024).

51. Lowekamp, B. C., Chen, D. T., Ibanez, L. & Blezek, D. The design of simpleitk. *Front. Neuroinformatics* **Volume 7 - 2013**, 10.3389/fninf.2013.00045 (2013).